Monthly Notices of the ROYAL ASTRONOMICAL SOCIETY
MNRAS **457,** 1468–1489 (2016) doi:10.1093/mnras/stv2996

Radial constraints on the initial mass function from TiO features and Wing–Ford band in early-type galaxies

Francesco La Barbera,[1⋆] Alexandre Vazdekis,[2,3] Ignacio Ferreras,[4] Anna Pasquali,[5] Michele Cappellari,[6] Ignacio Martín-Navarro,[2,3] Frederik Schönebeck[5] and Jesús Falcón-Barroso[2,3]

[1] *INAF–Osservatorio Astronomico di Capodimonte, sal. Moiariello 16, I-80131 Napoli, Italy*
[2] *Instituto de Astrofísica de Canarias, Calle Vía Láctea s/n, E-38205 La Laguna, Tenerife, Spain*
[3] *Departamento de Astrofísica, Universidad de La Laguna (ULL), E-38206 La Laguna, Tenerife, Spain*
[4] *Mullard Space Science Laboratory, University College London, Holmbury St Mary, Dorking, Surrey RH5 6NT, UK*
[5] *Astronomisches Rechen-Institut, Zentrum für Astronomie, Universität Heidelberg, Mönchhofstr. 12-14, D-69120 Heidelberg, Germany*
[6] *Sub-department of Astrophysics, Department of Physics, University of Oxford, Denys Wilkinson Building, Keble Road, Oxford OX1 3RH, UK*

Accepted 2015 December 22. Received 2015 November 22; in original form 2015 September 28

ABSTRACT

At present, the main challenge to the interpretation of variations in gravity-sensitive line strengths as driven by a non-universal initial mass function (IMF) lies in understanding the effect of the other population parameters. Most notably, [α/Fe]-enhanced populations or even departures in the *individual* element abundances with respect to the solar-scaled ratio may lead to similar observational results. We combine various TiO-based, IMF-sensitive indicators in the optical and NIR spectral windows, along with the FeH-based Wing–Ford band to break this degeneracy. We obtain a significant radial trend of the IMF slope in XSG1, a massive early-type galaxy (ETG), with velocity dispersion $\sigma \sim 300$ km s^{-1}, observed with the Very Large Telescope/X-shooter instrument. In addition, we constrain – for the first time – both the shape and normalization of the IMF, using only a stellar population analysis. We robustly rule out a single power law to describe the IMF, whereas a power law tapered off to a constant value at low masses (defined as a bimodal IMF) is consistent with all the observational spectroscopic data *and* with the stellar M/L constraints based on the Jeans anisotropic modelling method. The IMF in XSG1 is bottom-heavy in the central regions (corresponding to a bimodal IMF slope $\Gamma_b \sim 3$, or a mass normalization mismatch parameter $\alpha \sim 2$), changing towards a standard Milky Way-like IMF ($\Gamma_b \sim 1.3$; $\alpha \sim 1$) at around one half of the effective radius. This result, combined with previous observations of *local* IMF variations in massive ETGs, reflects the varying processes underlying the formation of the central core and the outer regions in this type of galaxies.

Key words: galaxies: elliptical and lenticular, cD – galaxies: formation – galaxies: fundamental parameters – galaxies: stellar content.

1 INTRODUCTION

Over the past few years, a number of papers have revisited the issue of the non-universality of the stellar initial mass function (IMF) in the unresolved stellar populations of early-type galaxies (ETGs). At present, there are three independent probes of the IMF in the unresolved, nearly quiescent populations of ETGs, based on the modelling of the kinematics (e.g. Cappellari et al. 2012; Dutton et al. 2013; Tortora, Romanowsky & Napolitano 2013), constraining the mass in strong gravitational lenses that probe the projected mass distribution in the central regions of galaxies (e.g. Auger et al. 2010; Ferreras et al. 2010; Treu et al. 2010), or via gravity-sensitive spectroscopic features (e.g. Cenarro et al. 2003; van Dokkum & Conroy 2010). The first two probes are sensitive to the stellar M/L, and their major systematic relates to the contribution of the dark-matter halo in the central regions of galaxies. Spectroscopic constraints are mostly sensitive to the ratio between giant and dwarf stars, and its main systematic is the degeneracy with the additional parameters of the underlying stellar populations, most notably the effect of variations in the individual elemental abundances. We focus here on this issue.

⋆ E-mail: flabarber@gmail.com

A large effort has been made to understand this systematic in detail. The bottleneck in the analysis is the lack of robust models of stellar atmospheres, and their response to abundance effects. On this front, population synthesis modellers follow either a theoretical approach (e.g. Conroy & van Dokkum 2012a) or an empirical methodology (e.g. Vazdekis et al. 2012). The theoretical approach relies on predictions from stellar atmosphere models to construct stellar population models that best match the observed spectra, while the empirical approach targets the deviation of the data from solar-scaled stellar population models to measure the abundance effects. At present, both methods are needed to be able to improve our understanding of line strengths in unresolved stellar populations. On the issue of IMF variations, a number of papers have recently strengthened the idea that ETGs feature a non-universal IMF (see Conroy & van Dokkum 2012b; Spiniello et al. 2014, as well as Ferreras et al. 2013; La Barbera et al. 2013, hereafter FER13 and LB13, respectively). Furthermore, the analysis has gone as far as providing tentative drivers of IMF variations, suggesting either [Mg/Fe] (Conroy & van Dokkum 2012b), velocity dispersion (Cappellari et al. 2013b; FER13; LB13), metallicity (Martín-Navarro et al. 2015c), or more complex physical observables (Spiniello et al. 2015a). Studies combining galaxy dynamics and spectroscopic features of the same galaxies have revealed potentially serious systematics (Smith 2014), although such effects could be strongly model-dependent (McDermid et al. 2014; La Barbera, Ferreras & Vazdekis 2015). In addition, constraints based on strong gravitational lensing are inconclusive: while Posacki et al. (2015) find agreement with the dynamical modelling, several massive lensing ETGs feature stellar M/L values consistent with a Kroupa-like IMF (Smith 2014; see also Smith & Lucey 2013). Critics have voiced concerns on the interpretation of the line-strength variations as an IMF trend, proposing instead large departures from the solar-scaled abundance of individual elements such as sodium (Jeong et al. 2013; Zieleniewski et al. 2015). It is therefore imperative to understand in detail the potential systematics (most notably, the effect of elemental abundances, age, and metallicity). On the spectroscopic analysis side – the focus of this paper – it is necessary to put under the microscope several spectral features, ideally with varying levels of dependence on the parameters under scrutiny.

The main target of the present work is a luminous ETG, hereafter XSG1, selected from the SPIDER survey (La Barbera et al. 2010b), more specifically from the subsample of 160 ETGs with $280 < \sigma < 320$ km s^{-1} defined by LB13. We have gathered new, very deep, 'high' resolution (>4000), long-slit spectroscopy for XSG1 with the X-shooter spectrograph on the ESO-Very Large Telescope (VLT). The combination of depth, resolution, and wavelength range for XSG1 gives us a unique opportunity to single out the effect of the IMF against the other stellar population parameters (in particular abundance ratios), as a function of galactocentric distance, advancing our previous work (Martín-Navarro et al. 2015a, hereafter MN15a). To this effect, we focus on the optical, TiO-based, spectral features, combining them with the near-infrared (NIR) TiO feature, TiO0.89, at $\lambda \sim 8860$ Å, and the Wing–Ford band, FeH0.99 ($\lambda \sim 9915$ Å).

The layout of the paper is as follows. In Section 2, we describe the observations and instrumental setup. Section 3 deals with the data reduction. The analysis is detailed in Section 4, including a description of the radial binning of the data (Section 4.1), the stellar population models used (Section 4.2), the determination of stellar age (Section 4.3), and abundance-ratio (Section 4.4) profiles, as well as the method to constrain the IMF (Section 4.5). Section 5 presents the main results of the work, i.e. the radial trends of IMF- and abundance-sensitive features in XSG1, for TiO features (Section 5.1) and the Wing–Ford band (Section 5.2), the inferred radial trend of IMF slope (Section 5.3), as well as constraints to the radial variation of IMF normalization, via a comparison of the stellar population analysis with dynamics (Section 5.4). A discussion is presented in Section 6, followed by a summary in Section 7.

2 OBSERVATIONS

The main target of the present work is XSG1 (SDSS J142940.63+002159.0), a massive ($M_\star \sim 2 \times 10^{11}\,M_\odot$; $\sigma \sim 300$ km s^{-1}) ETG at redshift $z \sim 0.057$, taken from the SPIDER survey (La Barbera et al. 2010b). The galaxy has been selected from the sample of LB13 to have a high abundance ratio ([α/Fe] ~ 0.4). Fig. 1 shows the r-band image of XSG1 drawn from the Sloan Digital Sky Survey (SDSS), together with the residual map obtained by fitting the galaxy surface brightness distribution with a two-dimensional, point spread function convolved, Sérsic model, using the software 2DPHOT (La Barbera et al. 2008). XSG1 is a round object ($b/a \sim 0.9$), whose light distribution is well described by a de

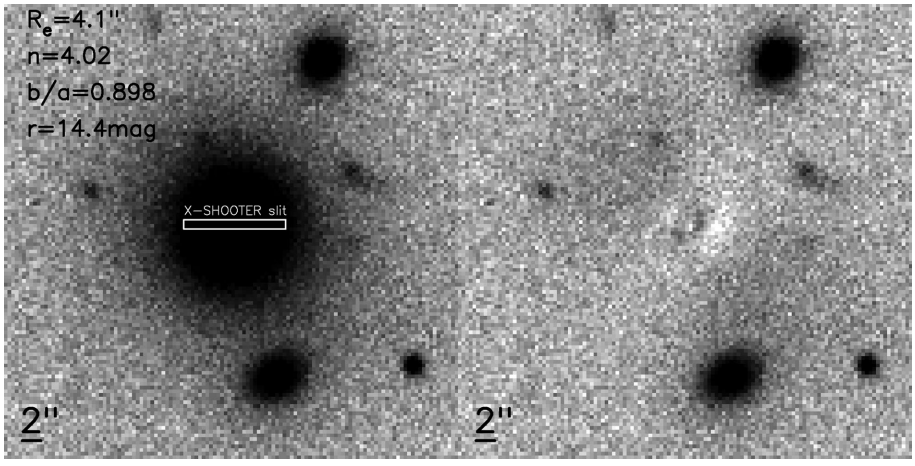

Figure 1. SDSS r-band image of XSG1 (top left). The X-shooter slit is overplotted as a white rectangle. North is right and east is up. The spatial scale (2 arcsec) is shown in the bottom-left corner. We include in this panel the effective radius, R_e, the Sérsic index, n, the axial ratio b/a, and the total r-band magnitude of the best-fitting Sérsic model. Top right: residual map, after subtracting the best-fitting Sérsic model.

Vaucouleurs profile, with best-fitting Sérsic $n \sim 4$, and an effective radius of $R_e \sim 4.1$ arcsec (see Fig. 1), consistent with the SDSS estimate of $r_{e,\,SDSS} \sim 4.4$ arcsec (based on a de Vaucouleurs model).

We have obtained new deep long-slit spectroscopy for XSG1 with the X-shooter spectrograph at the ESO-VLT, on Cerro Paranal (Proposal IDs: 092.B-0378, 094.B-0747; PI: FLB). X-shooter is a second-generation ESO-VLT instrument – a slit echelle spectrograph that covers a wide spectral range (3000–25 000 Å), at relatively high resolution (Vernet et al. 2011). The incoming bin is split into three independent arms (ultraviolet-blue, UVB: 3000–5900 Å; visible, VIS: 5300–10 200 Å; near-infrared, NIR: 9800–25 000 Å), each one equipped with optimized optics, dispersive elements, and detectors, ensuring high sensitivity throughout the entire spectral range. Observations were done through five observing blocks (OBs), each including two exposures on target, interspersed by two sky exposures (through an object–sky–sky–object sequence), with the same integration time as for the science target. For each OB, the on-target exposure time was 20.4, 22.6, and 25 min, resulting into a total exposure time of ∼1.7, 1.9, and 2.1 h, in the X-shooter UVB, VIS, and NIR arms, respectively. The observations were carried out in service mode during two consecutive nights at the end of 2014 March (four out of five OBs), and completed at the end of 2015 February. All data were taken under photometric conditions, with seeing FWHM (full width at half-maximum) varying from 0.7 to 1.1 arcsec in the optical, with a mean value of 0.9 arcsec. The X-shooter slit is 11 arcsec long, with a spatial scale of 0.16 arcsec pixel^{-1} in the UVB and VIS, and 0.21 arcsec pixel^{-1} in the NIR, arms. We adopted an instrument setup with 0.9-, 0.9-, and 1.0-arcsec-wide slits, providing a typical resolution power of $R \sim 4400$, ∼7500, and ∼5500, in the UVB, VIS, and NIR arms, respectively. The pointing was nodded by a few pixels along the slit among exposures, in order to perform an optimal removal of cosmic rays and detector defects (e.g. hot columns/pixels) during data reduction. A hot (white dwarf) spectrophotometric standard star, together with a few (3–7) telluric (B-type) standards, was observed during each night (the latter taken before and after each science OB) in order to perform flux calibration and correct the spectra for telluric lines, respectively.

As part of the same observing campaign as XSG1, we have also observed a second target, a massive ($M_\star \sim 1.2 \times 10^{11}\,M_\odot$; $\sigma \sim 300$ km s^{-1}) ETG (hereafter XSG2; SDSS J002819.30−001446.7; $z = 0.059$; $r_{e,\,SDSS} = 4.1$ arcsec) also selected from the SPIDER survey, with a more typical [α/Fe] (∼0.25 dex) for its velocity dispersion. XSG2 has been observed with X-shooter (Proposal ID: 094.B-0747; PI: FLB) through a series of 10 OBs, each consisting of an object–sky–object sequence. This different strategy, resulting into half of the total integration time spent on sky, allowed us to perform shorter individual exposures, in order to test the quality of sky subtraction in the NIR, where the fast variability of sky lines may hamper the analysis of the spectra, especially in the outer, low-surface-brightness regions. The data of XSG2 will be the subject of a forthcoming paper. Here, we only use the central spectrum of XSG2 to complement the analysis of the Wing–Ford band for XSG1, as detailed in Section 5.2.

3 DATA REDUCTION

The echelle layout of X-shooter produces 12–16 curved and highly distorted spectral orders per arm, requiring a complex reduction process. We refer the reader to Schönebeck et al. (2014) for a detailed description of all issues related to the data reduction of X-shooter UVB- and VIS-arm data. For our purposes, we performed the data reduction using version 2.4.0 of the X-shooter data-reduction pipeline (Modigliani et al. 2010), optimized with dedicated FORTRAN software developed by the authors. We ran the X-shooter pipeline in 'physical' mode, through the ESO command-line utility ESOREX. For each arm, the data (i.e. science and sky, as well as standard-star frames) were entirely pre-reduced with the X-shooter pipeline, including de-biasing, correction for dark frames (NIR-arm only), rectification of echelle orders, wavelength calibration, and merging of the orders. The remaining reduction steps were performed as follows.

Flux calibration – For the UVB and VIS arms, we found significant differences among reference spectra of standard stars to the flux-calibrated ones computed by the pipeline, being as high as 5–10 per cent in regions affected by strong telluric lines (for the VIS arm). For this reason, we applied an iterative procedure to improve the response function of the pipeline. The spectrum of each flux-calibrated standard star is corrected for tellurics with the same procedure as for the science data (see below). Then, for each echelle order, we derive the ratio of the corrected standard-star spectrum to its tabulated version. The ratio is fitted, order-by-order, with Legendre polynomials of suitable orders (from 1 to 12, depending on the spectral order), and the best-fitting polynomials are used to update the response function (for each observing night). The procedure is iterated a few times, until a variation below 1 per cent (the typical accuracy of our flux calibration) is achieved in the updated response function, at all wavelengths. For the NIR arm, the spectrum of the flux-calibrated standard star, produced by the pipeline, turned out to have large deviations (up to 10–15 per cent) with respect to the tabulated flux values. These deviations, with typical scales of ∼500 Å, are likely due to residual sky emission and telluric lines affecting the cubic-spline fit performed by the pipeline when deriving the response function. Therefore, we applied the flux calibration of the NIR arm with a dedicated procedure. For each observing night, the (one-dimensional) non-calibrated standard-star spectrum is corrected for tellurics with the software MOLECFIT (see below). Intrinsic (mostly hydrogen) absorption lines, from the stellar atmospheres, are removed, by fitting them with a linear combination of multiple Gaussian functions. We compute the ratio of the resulting spectrum to the tabulated one by carefully masking out regions with strong telluric absorption (>30 per cent) and removing pixels with spurious spikes (e.g. from cosmic rays or residuals of sky lines), through a 2σ clipping procedure. The resulting ratio is fitted with a second-order spline to produce an initial response function. This response is applied to each telluric standard star observed during the night. The continuum of the telluric standard is modelled, and removed, with two blackbody (BB) laws, one for bluer and another one for redder wavelengths with respect to the Brackett jump ($\lambda \sim 16\,000$ Å). The temperatures of the two BBs are obtained by a best-fitting procedure. The resulting signal, median-smoothed, and averaged over all telluric standards observed during the night, was applied as a correction to the initial response, to derive the final response function. Comparing the central spectrum of XSG1 among different exposures/nights, we have estimated that our NIR flux calibration is accurate at $\lesssim$2 per cent.

Sky subtraction – Our targets – with an effective radius around 4 arcsec – fill the whole X-shooter 11 arcsec slit. Therefore, sky subtraction cannot be performed in the standard way of interpolating the sky from the two sides of the slit. We performed sky subtraction with the software SKYCORR (Noll et al. 2014). Given the two-dimensional spectrum of the object, O, we consider the nearest sky frame, S. We extract a one-dimensional (1D) spectrum from

both *S* and *O*, by median-combining each frame over an 8 pixel region, using four pixels from each edge of the slit (where the signal from the galaxy is less prominent). We run SKYCORR to determine the optimal scaling factors (depending on wavelength) that match the 1D spectrum of the sky to that of the object frames. The scaling factors are then applied to re-scale *S*, and subtract it from *O*.

Telluric correction – Telluric lines were removed from each object exposure individually. For the VIS arm, we adopted two independent approaches, by (i) using telluric standard stars observed during our programme, and (ii) using the software MOLECFIT (Kausch et al. 2015; Smette et al. 2015). In case (i), we obtained, for each telluric standard star, an atmospheric transmission curve, by removing intrinsic absorption lines and the continuum from the stellar spectrum. The correction itself was performed by deriving the linear combination of (re-scaled) transmission curves that minimizes the absolute deviation to the object spectrum, computed over spectral regions with prominent telluric lines. In case (ii), MOLECFIT was run to compute a theoretical transmission model from the object spectrum itself. In general, both approaches were found to provide very consistent results (with differences below 1 per cent), as also shown in the analysis of line strengths throughout the present work. For the NIR arm, given the excellent quality of MOLECFIT fits, we decided to rely only on this method.

Combination – To combine different object exposures, we first aligned the photometric centre of the galaxy as a function of wavelength in each two-dimensional spectrum, in order to remove its spatial drift due to the atmospheric dispersion. To this effect, we collapsed the object spectrum along the slit direction in wavelength bins (with size ∼100 Å), and derived the photometric centre, for each bin, by fitting the collapsed profile with a linear combination of Gaussian functions. The aligned 2D spectra were then averaged with the IRAF tool *imcombine*. Cosmic rays, as well as pixels flagged by the X-shooter pipeline, were excluded from the average. A noise map was propagated accordingly.

4 ANALYSIS

4.1 Kinematics, JAM modelling, and radial binning

4.1.1 Kinematics

In order to compute the kinematics of XSG1, we binned the X-shooter two-dimensional spectrum along the spatial direction, starting from the photometric centre of the galaxy. We chose radial bins with a minimum width of 0.22 arcsec (i.e. about 1/4 of the seeing FWHM), and increased the bin width adaptively to reach a given, minimum (median) signal-to-noise ratio, S/N_{min} (computed per Å, at $\lambda \sim 4800$–5600 Å), in each bin. This procedure allowed us to reach an outermost radius of ∼0.88 (1.05) R_e for $S/N_{min} = 30$ (15). For each radial bin, we measured the recession velocity and the galaxy velocity dispersion using the software PPXF (Cappellari & Emsellem 2004), which simultaneously fits the stellar kinematics and an optimal linear combination of spectral templates to the observed spectrum, using a maximum-likelihood approach that works in wavelength space. We measured the kinematics independently in different spectral regions of the UVB and VIS arms ($\lambda = 4000$–9000 Å), combining the corresponding probability distribution functions into final estimates. From the recession velocity in the innermost bin, we obtain a redshift of $z = 0.055\,74 \pm 0.000\,01$ for XSG1, fully consistent with the value of $z = 0.055\,75 \pm 0.000\,01$ from the SDSS data base. Fig. 2 plots the profiles of

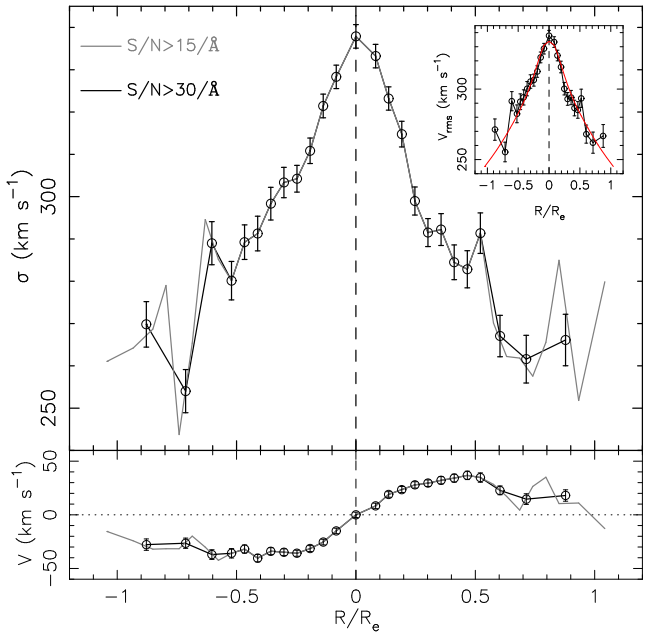

Figure 2. Velocity dispersion (top) and rotation velocity (bottom) profiles, obtained with PPXF, for XSG1, as a function of galactocentric distance, R/R_e. Black and grey curves correspond to radial binned spectra, along the X-shooter slit, with minimum S/N ratio of 30 and 15, respectively. Error bars denote 1σ uncertainties. Notice that the galaxy has low rotation, with a radial drop in velocity dispersion (from ∼340 km s^{-1} in the centre to ∼270 km s^{-1} at 1 R_e). The inset in the top panel compares the observed $V_{rms} = \sqrt{V^2 + \sigma^2}$ (open circles) with best-fitting results from the Jeans anisotropic modelling method (JAM, red curve in the inset; Cappellari 2008).

rotation velocity, *V*, and velocity dispersion, σ, for XSG1, showing that the galaxy is likely a pressure-supported system, with σ decreasing smoothly from ∼340 km s^{-1} in the centre to ∼270 km s^{-1} at 1 R_e, along both sides of XSG1. The galaxy rotation velocity is less than ∼50 km s^{-1} at all radii. Notice that we get very consistent kinematics when binning the spectra with either $S/N_{min} = 30$ or 15, as shown by the black and grey lines. Under the assumption of circular symmetry, the velocity dispersion profile in Fig. 2 implies a luminosity-weighted value $\sigma \sim 317$ km s^{-1} within the SDSS fibre aperture radius of 1.5 arcsec, consistent with two estimates of $\sigma = 301 \pm 9$ and 313 ± 10 km s^{-1} available from the SDSS data base.

4.1.2 JAM modelling

The inset in the top panel of Fig. 2 compares the observed rms velocity, $V_{rms} = \sqrt{V^2 + \sigma^2}$ (see open circles), with best-fitting predictions from the spherical version of the Jeans anisotropic modelling (JAM, red curve in the inset; Cappellari 2008). The use of a spherical model is motivated by the fact that above the critical mass $M \sim 2 \times 10^{11}$ $M_\odot$, ETGs are fully dominated by slow rotator galaxies, which are intrinsically quite close to spherical (Cappellari et al. 2013b). However, we also verified that, unlike the spherical model, an axisymmetric, intrinsically flat, but nearly face-on JAM model could not well describe the observed V_{rms} profile with a constant anisotropy, as one generally finds for fast rotators. Finally, from the V_{max}/σ_0 value computed from the long-slit spectrum, converted into $(V/\sigma)_e$ using equation 23 of Cappellari et al. (2007), the galaxy is securely classified as a slow rotator.

The JAM model is based on a Multi-Gaussian Expansion (MGE; Emsellem, Monnet & Bacon 1994) model of the SDSS *r*-band

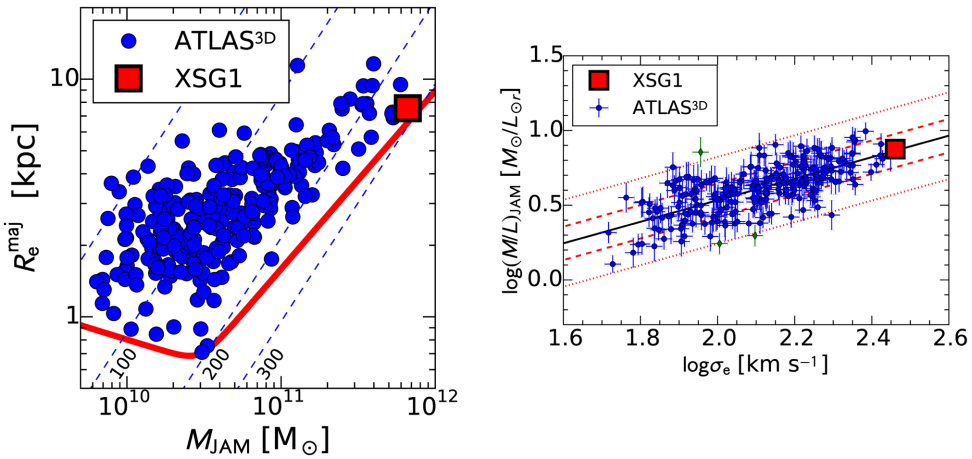

Figure 3. The ETG XSG1 (filled red square) is compared with the ATLAS^{3D} sample (blue dots; Cappellari et al. 2013a) by use of the JAM. Left: on the size–mass plane XSG1 represents a typical ETG at the massive end of the distribution. The dashed lines mark contours of constant velocity dispersion, as labelled (in km s^{-1}). The thick red line is the zone of exclusion, as given by equation 4 in Cappellari et al. (2013b). Note that the effective radius here is measured, for consistency, following the same methodology as in the ATLAS^{3D} sample (see the text for details). Right: the stellar r-band M/L derived from the JAM modelling makes XSG1 a typical massive ETG. The (1σ) error bars for XSG1 are smaller than the size of the square. The dashed and dotted red lines indicate the 1σ and 2.6σ (99 per cent) observed scatter around the best-fitting relation of the ATLAS^{3D} sample (black solid line).

image, using the PYTHON method and software of Cappellari (2002). The JAM model assumes that mass follows light,[1] within the region sampled by the kinematics, which implies that any possible dark matter within about 1 R_e is accounted for by a change in the total $(M/L)_{JAM}$. However, the dark-matter fraction is expected to be $\lesssim$30 per cent in the mass range (2×10^{11} M$_\odot$) of XSG1 (Cappellari et al. 2013a). The model adopts a supermassive black hole (SMBH) mass from the Kormendy & Ho (2013) SMBH–σ relation, and has a best-fitting radial anisotropy $\beta_r = 0.16$. This small and positive radial anisotropy is typical of slow rotators in the stellar mass range of XSG1 (Cappellari et al. 2007). The best-fitting total $(M/L)_{JAM}$, computed in the SDSS r band, is 7.50 ± 0.75. The error bar on $(M/L)_{JAM}$ is not just a formal error but is a quite conservative estimate, accounting for possible systematics in the modelling. Notice that the SMBH value is not critical in the derivation of $(M/L)_{JAM}$, but not completely negligible either. A model without an SMBH would give nearly the same $(M/L)_{JAM}$, but would require a larger anisotropy.

Fig. 3 compares XSG1 with respect to the local sample of ETGs from the ATLAS^{3D} survey (Cappellari et al. 2013b). The position of our galaxy both on the mass–size plane (left-hand panel) and the total (M/L) versus σ_e relation (right) is representative of a typical massive ETG. Notice that for this analysis, we follow, for consistency, the same procedure adopted by Cappellari et al. (2013a). In particular, we calculate the $R_e = 5.17$ arcsec as the radius enclosing half of the analytic MGE total light. This value is then multiplied by the factor 1.35 to bring it into consistency with the RC3 system (see fig. 7 of Cappellari et al. 2013a). This scaling factor is not universal, but it is justified by the facts that we are using the same kind of photometry as in the ATLAS^{3D} work. For a flat universe (Λ cold dark matter with $\Omega_m = 0.3$ and $H_0 = 70$ km s^{-1} Mpc^{-1}), this result maps into a physical effective radius of $R_e = 7.6$ kpc. Note that this is the value adopted, for consistency, when comparing with the ATLAS^{3D} sample (Fig. 3), in contrast with $R_e = 4.1$ arcsec (4.4 kpc) derived in Section 2 from a Sérsic fit to the SDSS r-band surface brightness profile. Note that in the rest of the paper, we use the latter as the fiducial value for R_e.

[1] Notice that although the assumption of (total) mass following light might be inconsistent with the finding that the stellar M/L varies with radius (see Section 5.4), as shown in fig. 9 of Cappellari et al. (2013a), the $(M/L)_{JAM}$ is actually robust against different assumptions, such as the inclusion of a more realistic [NFW (Navarro, Frenk, and White 1996)] dark-matter halo, in the modelling.

4.1.3 *Radial binning for stellar population analysis*

To constrain the IMF at different galactocentric distances, we construct six radially binned spectra, folding up the spectra from the opposite sides of the slit around the photometric centre. To this effect, we offset each row in the two-dimensional spectrum to the rest frame, adding up the spectra in radial bins. The bin width is increased adaptively, if needed, in steps of 0.225 arcsec (1/4 of the seeing FWHM), targeting an S/N > 90 per radial bin. In order to minimize seeing effects, the innermost spectrum has a width of 1.3 arcsec (i.e. $\pm$0.675 arcsec) around the photometric centre, corresponding to 1.5 times the mean seeing FWHM of our data. The outermost bin reaches an average galactocentric distance of $\sim$2/3 R_e. Since the velocity dispersion is one of the main parameters to interpret stellar populations via line strengths, we have re-run PPXF on the six binned spectra to get an accurate velocity dispersion estimate for each bin. The main characteristics of the spectra, i.e. radial range, average galactocentric distance, median S/N, and σ, are summarized in Table 1. Fig. 4 shows the six binned spectra of XSG1, zooming into those regions used to constrain the IMF in the present work.

4.2 Stellar population models

We analyse the X-shooter spectra with extended-MILES stellar population models (Röck et al. 2015; Röck et al., in preparation), the first set of single-burst stellar population models to date that cover both the optical and infrared wavelength range, between 3500 and 50 000 Å, based exclusively on empirical stellar spectra. These models combine MIUSCAT stellar population models (Ricciardelli et al. 2012; Vazdekis et al. 2012), covering the spectral range λ3465–9469 Å at a nominal resolution of 2.51 Å FWHM

Table 1. Relevant properties of radially binned spectra used to constrain the IMF. For all bins, we fold up the spectra around the photometric centre of the galaxy.

Radius (arcsec) (1)	Radial range (arcsec) (2)	σ (km s^{-1}) (3)	S/N (4)
0.0	[−0.675, +0.675]	333 ± 3	320
0.7875	[0.675, 0.900]	316 ± 3	130
1.025	[0.900, 1.150]	307 ± 3	110
1.3250	[1.150, 1, 500]	302 ± 3	100
1.7750	[1.500, 2.050]	291 ± 3	90
3.1250	[2.050, 4.200]	276 ± 3	90

(Falcón-Barroso et al. 2011), with the NIR model extension based on the Infrared Telescope Facility (IRTF) stellar library, covering the λ8150–50 000 Å wavelength range at a spectral resolution of 2000 (Röck et al. 2015). The MIUSCAT and IRTF models are joined in the interval λ8950–9100 Å. For λ < 8950 Å, the model predictions are identical to MIUSCAT. The extended-MILES models rely on solar-scaled isochrones with stellar spectra following the abundance pattern of our Galaxy, i.e. approximately solar-scaled at solar metallicity, and are derived from either Padova00 or BaSTI isochrones. For comparison with our previous works (e.g. FER13; LB13; MN15a), we base our analysis, throughout the present work, on Padova models. Because of the IRTF implementation, the extended-MILES Simple Stellar Populations (SSPs) cover a restricted parameter range than MILES models, i.e. ages from 1.0 to 17.78 Gyr, and four bins of total metallicity, i.e. $[M/H] = \{-0.71, -0.4, 0, +0.22\}$. The SSPs are provided for several IMFs, as for MILES models, i.e. unimodal (single power law) and bimodal (low-mass tapered) IMFs, both characterized by their slope, Γ (unimodal) and Γ_b (bimodal), as a single free parameter (see, e.g., Vazdekis et al. 1996, 2003; Ferreras et al. 2015). The bimodal IMFs are smoothly tapered off below a characteristic 'turnover' mass of 0.6 $M_\odot$. For $\Gamma_b \sim 1.3$, the bimodal IMF gives a good representation of the Kroupa IMF, while for $\Gamma \sim 1.3$ the unimodal IMF coincides with the Salpeter (1955) distribution. The lower and upper mass cutoff of the IMFs are set to 0.1 and 100 $M_\odot$, respectively. Notice that younger ages, as well as lower metallicities, than those provided by extended-MILES models are not relevant to the study of massive ETGs, while a mild extrapolation of the models to higher metallicity (from $[M/H] \sim +0.22$ up to $\sim+0.25$) is required to match the innermost spectrum of XSG1 (see Section 4.3). As in FER13 and LB13, we consider bimodal IMF models with $\Gamma_b = \{0.3, 0.8, 1.0, 1.3, 1.5, 1.8, 2.0, 2.3, 2.8, 3.3\}$, while for unimodal IMFs, we restrict the analysis to $\Gamma \leq 2.3$, where model predictions are safe (see Vazdekis et al. 2012).

To estimate the effect of abundance ratios on line strengths, we also combine the predictions of extended-MILES models, with those from other two sets of models, i.e. α-MILES (Vazdekis et al. 2015, hereafter VAZ15) and Conroy & van Dokkum (2012a, hereafter CvD12) SSPs. The α-MILES SSPs, having a spectral resolution of 2.51 Å (FWHM), are based on the MILES library and apply corrections from theoretical models of stellar atmospheres to produce spectra of old- and intermediate-age stellar populations with varying total metallicity, IMF, and [α/Fe] abundance ratios. The models are based on BaSTI scaled-solar and α-enhanced isochrones. The CvD12 models combine optical (MILES) and NIR (IRTF) empirical stellar libraries to produce integrated light spectra, at λ = 0.35–2.4 μm, with a resolving power of $R \sim 2000$. The empirical CvD12 models, computed at solar metallicity and in the age range from 3 to 13.5 Gyr, are complemented with synthetic SSPs modelling the spectral variations due to changes in individual elemental abundances, as well as in generic α-elements. We notice that CvD12 models are computed at fixed [Fe/H], rather than [M/H] (adopted in the extended- and α-MILES models), and based on a combination of three different sets of scaled-solar isochrones. We also emphasize that in the publicly available version of CvD12 models, SSPs with varying elemental abundances are only provided for a specific age (13.5 Gyr)

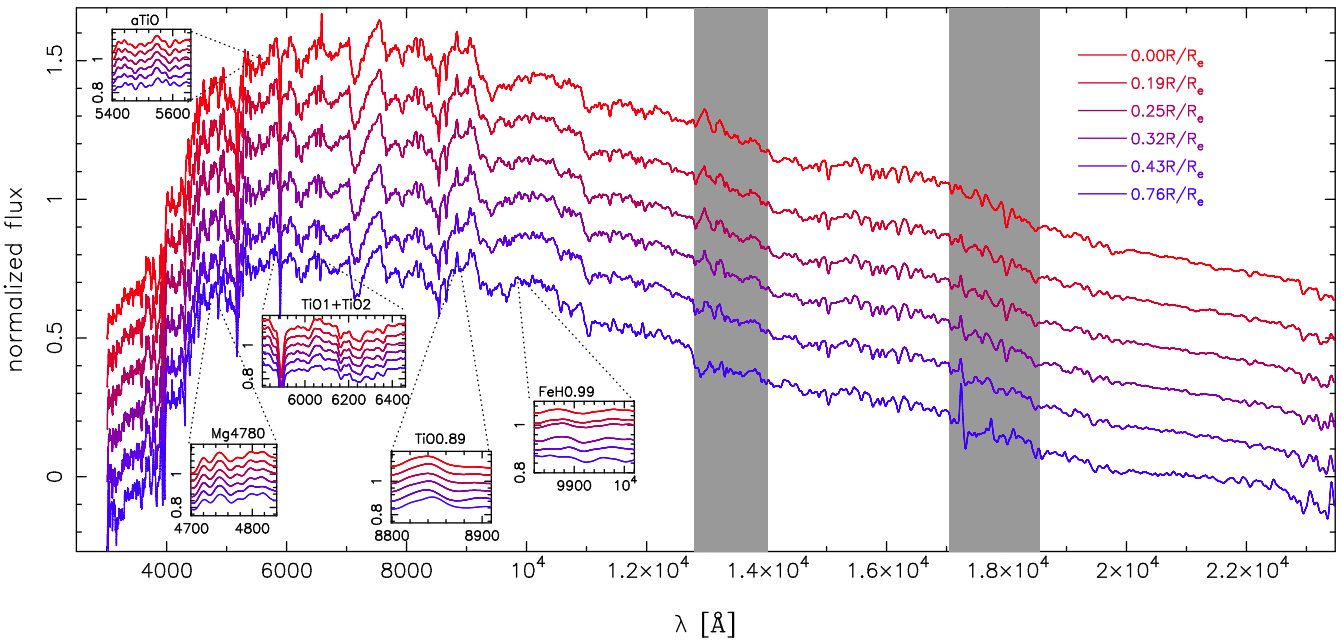

Figure 4. X-shooter spectra of XSG1 used to constrain the IMF. The data are radially binned in six galactocentric distances, out to $R/R_e \sim 0.8$. Different colours, from red through blue, correspond to different radial positions, as labelled. The insets are zoomed-in versions of the main spectral features used in the present work (see Section 4.5). All spectra have been smoothed, for displaying purposes, to a common velocity dispersion of 400 km s^{-1}.

and IMF (Chabrier), and [Fe/H] = 0. Because of the difference between α-MILES as well as CvD12 models and our reference extended-MILES SSPs (i.e. different isochrones, metallicity range, etc.), we use these other models mostly to perform a qualitative analysis of the data, whereas the quantitative results presented in this work (e.g. Section 5.3) are entirely based on extended-MILES models.

Notice that the present work relies on the analysis of line strengths, based on several index–index diagrams (see Section 5). In these diagrams – mostly used for illustrative purposes – all model line strengths are computed after smoothing the models to a σ of 300 km s^{-1} (accounting for the intrinsic spectral resolution of the models), i.e. the averaged velocity dispersion (among radial bins) for XSG1. In all index–index diagrams, observed line strengths are corrected to a common σ of 300 km s^{-1}. For a given radial bin, the correction is obtained using the corresponding best-fitting extended-MILES SSP (see Section 5.3). We compute the difference of each line strength when smoothing the model to the actual σ of the spectrum and the reference value of 300 km s^{-1}. Given the relative narrow range in velocity dispersion for XSG1, and the fact that we mostly analyse broad features (e.g. TiO and FeH0.99), the correction is largely independent of the specific model (e.g. age and metallicity) adopted. However, in our quantitative analysis (i.e. when fitting model to observed line strengths), we compute, for each bin, line strengths at the original σ of the data, and smooth the models accordingly. We prefer this approach, rather than smoothing all observed spectra to the same σ, as it extracts the maximum amount of information from the data (see, e.g., LB13), and avoids any contamination of the relevant features, when smoothing the spectra, from nearby sky residuals.

4.3 Radial profiles of age and metallicity

An accurate estimate of age and metallicity is needed to constrain the IMF, because gravity-sensitive spectral features also depend, to some extent, on such parameters. We estimate radial profiles of age and [M/H] for XSG1 with different methods, as illustrated in Fig. 5. In particular, regarding stellar age, we explore several approaches (see labels in the top panel of the figure).

FIT1 – The age is derived by performing spectral fitting over the wavelength range λ = 3800–6200 Å. The fit is done individually for extended-MILES SSPs with different choices of Γ_b (see Section 4.2), normalizing both model and observed spectra by the median flux in a reference spectral window (λ = 5200–5400 Å). The black solid line in the figure plots the median age value, for each radial bin, among SSPs with different Γ_b. The black error bars reflect the statistical uncertainty on the age, summed in quadrature to the standard deviation among estimates for different values of the IMF slope, Γ_b. We find no significant age gradient throughout the galaxy. This result is further confirmed when fitting models with extended star formation histories to the spectra (see FER13 and LB13 for details), in which case we find very small differences ($\lesssim$0.2 Gyr) between luminosity- (as well as mass-) weighted ages with respect to the results with SSP models, meaning that at all radial bins the spectra of XSG1 are very well described by a single SSP. This is consistent with the high [α/Fe] (implying a very short star formation time-scale in the galaxy within the effective radius, see below). The dotted and dashed black lines in the top panel of Fig. 5 show the results for a Kroupa-like (Γ_b = 1.3) and a bottom-heavier (Γ_b = 3) IMF, showing that, for our X-shooter data, the age profile does not depend on Γ_b. On the other hand, we found that the absolute

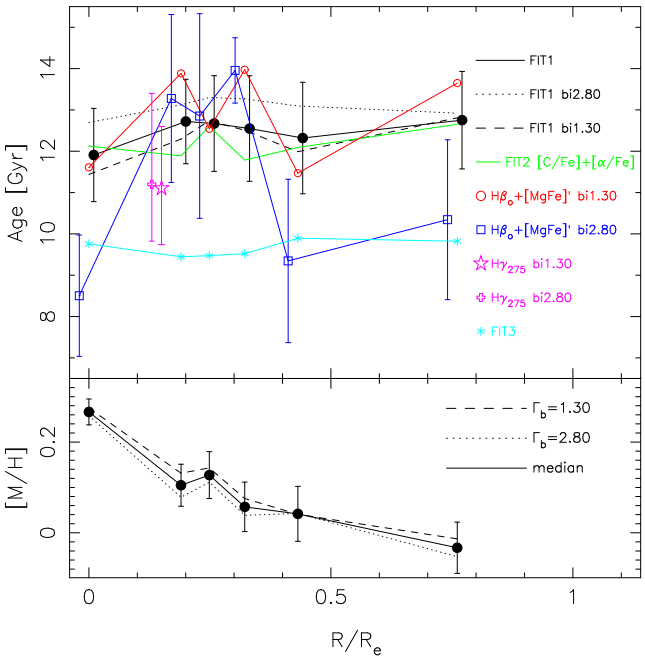

Figure 5. Radial trends of age (top) and metallicity (bottom) in XSG1. Different symbols and line types correspond to different methods to derive age and metallicity, as labelled (see the text for details). Error bars denote 1σ uncertainties.

value of the age depends on the adopted methodology, e.g. the way one normalizes the continua of observed and model spectra prior to spectral fitting. The cyan profile in the figure (labelled FIT3) shows the case when one divides the spectra by their integrated flux in the normalization window (see above), rather than the median flux (as for the solid black curve). Although the age gradient does not change, we find an overall shift of $\sim$2 Gyr in the age values. In general, changing the setup of the spectral fitting approach (e.g. the continuum normalization window), we found variations in the mean age from 10 to 13 Gyr.

FIT2 [C/Fe] + [α/Fe] – The solid green line in the top panel of Fig. 5 shows the spectral fitting constraints when 'removing' the effect of [C/Fe] and [α/Fe] abundance ratios from the observed galaxy spectrum at each radial bin. In practice, for each radial bin, we use CvD12 SSP models to estimate the ratio of [C/Fe]- and [α/Fe]-enhanced SSPs with respect to the solar-scaled SSP, and divide the observed spectrum by this ratio. The ratio is estimated using the median values of [C/Fe] and [α/Fe] measured for each bin (Section 4.4). Notice that we consider here only the effect of [C/Fe] and [α/Fe] as (i) both turn out to be enhanced in XSG1, (ii) they are the leading abundances to affect the TiO-based optical features analysed in the present work (see Section 5.1), and (iii) CvD12 models suggest that [α/Fe] and [C/Fe] are the main abundance ratios whose enhancement affects the shape of the continuum, possibly leading to a biased determination of age from spectral fitting. Notice that enhancing [α/Fe] tends to make a given spectrum bluer, mimicking the effect of a young age (see, e.g., VAZ15). In contrast, enhancing [C/Fe] tends to counteract this effect (i.e. reddening the spectrum; see Lee, Worthey & Blakeslee 2010). As a result, for XSG1, accounting for the effect of abundance ratios does not change the age determination with respect to solar-scaled models.

Hβ_o – We use predictions from MILES SSP models to fit simultaneously the Hβ_o age-sensitive indicator (Cervantes & Vazdekis 2009)

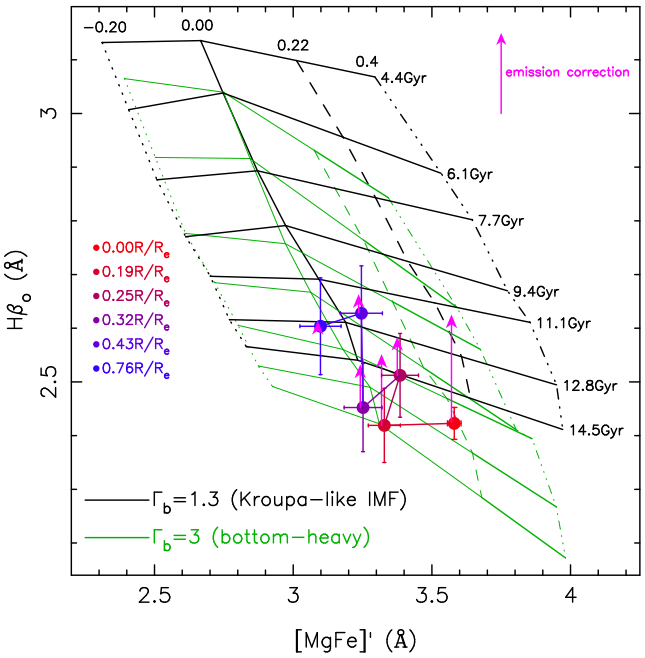

Figure 6. The age indicator Hβ_o is plotted as a function of the total metallicity index [MgFe]′. The solid dots represent the observed line strengths in XSG1 (1σ error bars), corrected to a common velocity dispersion of 300 km s^{-1} (see Section 4.2). The black and green grids correspond to Kroupa-like ($\Gamma_b = 1.3$) and bottom-heavy (bimodal IMF; $\Gamma_b = 3$) MILES model predictions with varying age and metallicity, as labelled. Notice that, for the specific purpose of this plot, the grids have been linearly extrapolated from the maximum value of [M/H] = +0.22 in MILES models up to [M/H] = +0.4. Different radial bins are shown (inside-out) with red-through-blue colours (see labels on the left side of the plot). The effect of emission line correction on Hβ_o is shown with magenta arrows.

and the total metallicity indicator [MgFe]′ (Thomas, Maraston & Bender 2003). The equivalent widths (EWs) of Hβ_o are corrected for emission contamination as described in LB13, i.e. estimating the excess of flux in the line with respect to a combination of two SSPs that gives the best fit in the Hβ spectral region (λ = 4530–4730 Å) after excluding the trough of the absorption. The correction to Hβ_o varies from ∼0.2 Å in the innermost bin to less than ∼0.05 Å in the outermost regions. Fig. 6 shows the radial variation of Hβ_o and [MgFe]′ line strengths in XSG1. The corrected values of Hβ_o suggest no significant radial gradient in XSG1, as confirmed by the age trend inferred for a Kroupa-like IMF from the Hβ_o–[MgFe]′ diagram (red solid line in top panel of Fig. 5). Notice, however, that MILES models predict a decrease of Hβ_o with IMF slope, as seen by comparing green versus black grids in Fig. 6, corresponding to models with Γ_b = 3 and 1.3, respectively (see LB13 and VAZ15 for more details). As a result, for a bottom-heavy IMF, one infers younger ages than for a Kroupa-like distribution (see the blue solid line in the top panel of Fig. 5).

Hγ_{275} – By summing up the three innermost galaxy spectra of XSG1, the median S/N in the Hγ spectral region ($\lambda \sim$ 4340 Å) is high enough (>350) to constrain the age with the Hγ_{275} spectral index, proposed by Vazdekis & Arimoto (1999, see also Yamada et al. 2006). This index is a pure age indicator, i.e. it is completely independent of metallicity (provided that the wavelength calibration is accurate enough, as is the case for our X-shooter data). The magenta symbols in the top panel of Fig. 5 show the age inferred from Hγ_{275} when using either Kroupa-like (Γ_b = 1.3) or bottom-heavy (Γ_b = 3) SSP models. The age inferred in the galaxy centre from Hγ_{275} (∼11 Gyr) is independent of the IMF, and is consistent with those obtained from spectral fitting (∼10–12 Gyr, see the black and cyan lines in the figure).

In summary, our analysis shows that the spectra of XSG1 feature homogeneously old stellar populations inside the effective radius, with no significant age gradient. The absolute value of the age depends on the methodology, a well-known issue plaguing most stellar population studies (see, e.g., Vazdekis et al. 2001; Schiavon et al. 2002). Throughout this work, we adopt as a reference the age estimates from spectral fitting (method FIT1 above), re-scaled to match the Hγ_{275}-based value (∼11 Gyr) at the galaxy centre. We stress that this assumption serves only for illustrative purposes (e.g. to estimate the metallicity and abundance-ratio gradients of XSG1), while in practice, when constraining the IMF, our fitting scheme takes into account the uncertainties on the age zero-point with an ad hoc procedure (see Section 4.5).

The bottom panel of Fig. 5 shows the metallicity profile for our reference age estimates, from the [MgFe]′ index. The [MgFe]′ is largely independent of IMF slope, implying that, *at fixed age*, metallicity estimates are independent of the IMF (see the dotted and dashed black lines in the figure). Notice that [MgFe]′ is also well known for being independent of [α/Fe] (Thomas, Maraston & Bender 2003; Thomas, Maraston & Johansson 2011; VAZ15). Moreover, CvD12 models predict a small variation of [MgFe]′ with non-alpha elements (e.g. δ[MgFe]′ ∼ − 0.03 Å for δ[C/Fe] = +0.15 dex,[2] at σ = 300 km s^{-1} and for an age of 13.5 Gyr). Hence, after accounting for the uncertainty on the zero-point of the age, the [M/H] can be robustly constrained from [MgFe]′. Fig. 5 shows that XSG1 has a negative metallicity gradient of about −0.25 dex per radial decade, a typical value in massive ETGs (e.g. Sánchez-Blázquez et al. 2007; Spolaor et al. 2010).

4.4 Radial profiles of abundance ratios

Deviations from the solar scale of the abundance ratios involving single elements can partly mimic (or mask out) the effect of a varying IMF on gravity-sensitive features (see CvD12). Since TiO features, which are the main focus of the present study, are mainly affected by [C/Fe] and [α/Fe] (see Section 5.1), in the present section we analyse the radial gradients of [C/Fe] and [α/Fe] in XSG1, pinpointing the uncertainties arising from different model assumptions. Notice that we do not aim at obtaining a precise, quantitative, determination of abundance ratios, but rather to perform a qualitative characterization of the radial behaviour of [α/Fe] and [C/Fe] in XSG1.

Fig. 7 plots different estimates of [α/Fe] and [C/Fe] (i.e. different methods/models; see lines with different colours) as a function of galactocentric distance. The solid red-through-blue line, joining filled circles, shows our solar-scaled proxy for [α/Fe], measured as a difference between the metallicity estimates derived, at fixed age, from Mg*b*5177 and Fe3. The proxy has been calibrated on to [α/Fe] with the aid of Thomas et al. (2011, hereafter TMJ11) stellar population models, as detailed in LB13 (see also VAZ15), resulting into an accuracy (rms) of only 0.025 dex in [α/Fe]. The dotted and dashed lines in Fig. 7 also show [α/Fe] and [C/Fe] obtained by fitting simultaneously [MgFe]′, Mg*b*5177, Fe3, and C4668 line

[2] It is important to remind the reader that these predictions hold at fixed [Fe/H] = 0, and assume no effect from varying abundance ratios on the solar-scaled isochrones.

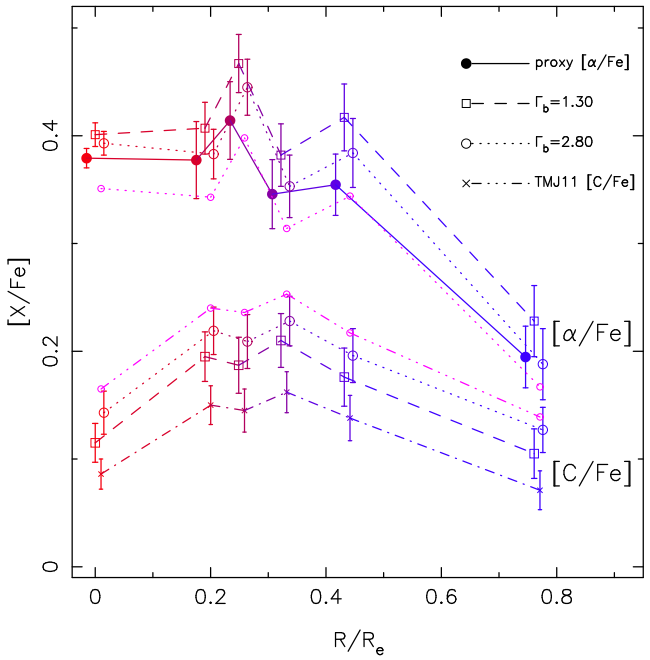

Figure 7. Radial trends of elemental abundance ratios in XSG1. We plot [C/Fe] and [α/Fe] abundance ratios. These are expected to contribute the most to variations in the TiO features (see the text, and Fig. 8). The upper (lower), red-through-blue, curves plot the [α/Fe] ([C/Fe]) radial trends, respectively, as labelled. Different line types correspond to different methods to estimate the abundance ratios (see the labels on the upper-right corner of the bottom panel). Error bars are quoted at the 1σ level.

strengths with predictions from MILES models with a Kroupa-like ($\Gamma_b = 1.3$) and a bottom-heavy ($\Gamma_b = 3$) IMF, respectively. The fit is done by minimizing the rms scatter of model and observed line strengths with respect to [C/Fe] and [α/Fe] (see equation 1 in Section 4.5), where the sensitivity of line strengths to [α/Fe] ([C/Fe]) is computed with α-MILES (CvD12) stellar population models, for old (13.5 Gyr) age and solar metallicity. The reason for adopting Mg*b*5177 and Fe3 is that these features are strongly sensitive to [Mg/Fe], while C4668 is extremely sensitive to carbon abundance (e.g. Tripicco & Bell 1995). The pink dotted lines in Fig. 7 are the same as the red-through-blue dotted lines, but estimating the sensitivity of Mg*b*5177, Fe3, and C4668 to [α/Fe] in the fitting with $\alpha-$MILES SSPs having super-solar ([M/H] = +0.26), rather than solar (see above) metallicity. In this case, C4668 decreases more with [α/Fe] than for [M/H] = 0, implying higher inferred values of [C/Fe]. Notice also that, as mentioned above, CvD12 models are computed at fixed [Fe/H], rather than total metallicity. Hence, combining CvD12 and extended-MILES model predictions is only meaningful for elements that give a negligible contribution to [M/H]. Since this is only approximately true for [C/Fe], we have also repeated the fits by modelling the sensitivity of C4668 to carbon with TMJ11 models (computed at fixed [M/H]). As shown by the dot–dashed line in Fig. 7, the TMJ11 models, relative to CvD12, lead to lower [C/Fe] estimates, by ∼0.05 dex (compare the dot–dashed versus dashed curves in Fig. 7).

Fig. 7 shows that there is good agreement among estimates of [α/Fe] from different methods, with differences below ∼0.08 dex for each radial bin. In particular, changing Γ_b (dotted versus dashed red-through-blue curves) gives differences $\lesssim$0.05 dex, implying that the derivation of [α/Fe] is robust with respect to the assumed IMF slope. We find that the radial profile of [α/Fe] in XSG1 is essentially constant with radius, out to one half of the effective radius, with a very high [α/Fe] (∼+0.4), and decreases to ∼0.2, only in the outermost bin. Regarding [C/Fe], differences among methods are more significant (up to 0.1 dex) than for [α/Fe]. In general, we find that, similar to [α/Fe], [C/Fe] is approximately constant with radius (∼0.2 dex), at least in the radial range from 0.2 to 0.5 R_e, dropping to ∼0.1 dex at the largest distance probed (∼0.8R_e). Notice that although the decrease of [C/Fe] in the innermost radial bin might be due to model uncertainties in the high-metallicity regime, in practice such a trend does not affect at all our IMF constraints (Section 5.3). Also one can notice that, with the exception of the innermost bin, the ratio of [α/Fe] to [C/Fe] throughout the galaxy is approximately constant (∼2). The radial behaviour of [α/Fe] and [C/Fe] has important implications for the analysis of TiO-based gravity-sensitive features, as discussed below, in Section 5.1.

4.5 Constraining the IMF slope

4.5.1 Fitting scheme

The approach we adopt to constrain the IMF is an improved version of the method developed in our previous works (e.g. FER13; LB13; MN15a; Martín-Navarro et al. 2015b,c). For each radial bin of XSG1, we minimize the following expression,

$$\chi^2(\mathrm{IMF}, t_M, [M/H], [X/Fe]_r) = \left[\frac{\mathrm{Age} - \mathrm{Age_M}}{\sigma_{\mathrm{Age}}}\right]^2 + \sum_i \left[\frac{E^{ss}_{O,i} - E_{M,i}}{\sigma_{E^{ss}_{O,i}}}\right]^2, \quad (1)$$

where the summation index i runs over a selected set of spectral features (see Section 4.5.2), Age and σ_{Age} are our reference estimates of the age (updated through an iterative procedure; see Section 4.5.3) and its uncertainty for the given spectrum (Section 4.3), $E_{M,i}$ are line-strength predictions for an SSP model with age $\mathrm{Age_M}$, $E^{ss}_{O,i}$ are observed line strengths – $E_{O,i}$ – corrected to solar scale with an approach similar to that of LB13, i.e.

$$E^{ss}_{O,i} = E_{O,i} - C_i(Z_{MW}) \cdot [\alpha/\mathrm{Fe}], \quad (2)$$

where $C_i(Z_{MW})$ is the *observed* slope of the correlation between a given index line strength and [α/Fe], derived from SDSS data (see LB13). Z_{MW} represents the total metallicity, estimated for a Milky Way (MW)-like IMF (in practice, we use a bimodal IMF with Γ_b = 1.3) from the (emission-corrected) Hβ_o versus [MgFe]′ diagram (see, e.g., Fig. 6). The uncertainty, $\sigma_{E^{ss}_{O,i}}$, is obtained by adding in quadrature the statistical error on $E_{O,i}$ with the uncertainty on the solar-scaled correction (see section 6 of LB13).

Notice that our IMF constraints for XSG1 rely on the use of single SSP models to fit observed line strengths (equation 1). As discussed in Section 4.3, this assumption is well motivated from results of spectral fitting, as well as from the high values of [α/Fe] for XSG1, pointing to homogeneously old ages for this galaxy at all radii. Moreover, as discussed in LB13, the use of complex star formation histories (e.g. 2SSP models) does not affect significantly the derived IMF slopes in ETGs with high velocity dispersion, while the effect is measurable, although mild, in ETGs with low velocity dispersion. We note that spectral fitting (see FIT1 in Section 4.3) yields probability distribution functions at all radii with a negligible fraction in young (<8 Gyr) components. In MN15a, we explicitly show that the use of multiple SSP models does not change the radial profile of the IMF slope in the elliptical galaxy NGC 4552 whose velocity dispersion is comparable to that of XSG1.

Table 2. Targeted spectral indices applied to constrain the IMF. Wavelengths are quoted in the air system. Notice that the TiO0.89 index has no units, as it is defined as a flux ratio between the blue and red passbands.

Index	Units	Blue pseudo-continuum (Å)	Central feature (Å)	Red pseudo-continuum (Å)	Ref.
(1)	(2)	(3)	(4)	(5)	(6)
Mg4780	Å	4738.9–4757.3	4760.8–4798.8	4819.8–4835.5	Serven+05
TiO1	mag	5816.625–5849.125	5936.625–5994.125	6038.625–6103.625	Trager+98
TiO2	mag	6066.625–6141.625	6189.625–6272.125	6422.0–6455.0	LB13
aTiO	mag	5816.625–5849.125	5936.625–5994.125	6038.625–6103.625	STK14
TiO0.89		8832.569–8852.563		8867.559–8887.554	CvD12
FeH0.99	Å	9852.292–9877.285	9902.278–9932.270	9937.268–9967.260	CvD12

4.5.2 *Selected spectral features*

The definition of the main spectral features used in the present work is summarized in Table 2. We focus on optical (mostly TiO-based) gravity-sensitive features, i.e. TiO1, TiO2, aTiO, and Mg4780,[3] contrasting the constraints from these features with those from the Wing–Ford band (hereafter FeH0.99) in the NIR ($\lambda \sim 0.992$ μm). Moreover, we include the total metallicity indicator, [MgFe]′, in our χ^2 minimization procedure. Since [MgFe]′ is independent of abundance ratios (see, e.g., TMJ11; VAZ15), for this index we set $C_i(Z_{\rm MW}) = 0$ in equation (1). Hence, the input of our fitting procedure consists of empirically corrected values of TiO1, TiO2, aTiO, Mg4780, plus [MgFe]′ and our reference Age estimates. Given this input, we minimize equation (1) over a set of extended-MILES models, deriving the best-fitting values of the relevant model parameters, and in particular the IMF slope, i.e. Γ ($\Gamma_{\rm b}$) for unimodal (bimodal) models.

Notice that for FeH0.99, no empirical correction is available at the moment, and thus the fitting is performed in a different manner, relying on theoretical (CvD12) models alone to estimate the impact of abundance ratios (see Section 5.2 for details). In addition to TiO1, TiO2, aTiO, Mg4780, and FeH0.99, we also study the radial behaviour of the NIR TiO feature, TiO0.89 ($\lambda \sim 0.886$ μm), defined by CvD12. This feature is mostly sensitive to abundance ratios as well as giant (rather than both dwarf and giant) stars in the IMF (in contrast to most TiO lines), and has been recently used, for similar purposes as in our work (i.e. studying IMF and abundance-ratio gradients), by McConnell, Lu & Mann (2015). These authors combined TiO0.89 with gravity-sensitive features arising from different elements (Na and Fe) than TiO. To our knowledge, the present work is the first one where optical and NIR TiO features – sensitive to the *same* elemental abundances ([Ti/Fe] and [O/Fe]; see Section 5.1) – are studied simultaneously to constrain the IMF. Combining TiO0.89 with features sensitive to temperature – and in particular the optical TiO-related indices – allows us to disentangle the contribution of giants and abundance ratios, with respect to dwarfs, in the line strengths. Notice that while we discuss the radial behaviour of TiO0.89, we do not include it into our χ^2 minimization procedure (equation 1), as we fit IMF slope, age, and metallicity, but not abundance ratios, to the (solar-scale corrected) line strengths. Indeed, obtaining a precise determination of abundance ratios is not the main purpose of the present work.

[3] We notice that a very similar index as Mg4780, named bTiO, has been defined by Spiniello et al. (2014) to constrain the IMF. In practice, bTiO and Mg4780 have a very similar sensitivity to IMF, and abundance ratios.

4.5.3 *Novelties in the approach*

The approach adopted in the present work (equation 1) has some relevant difference with respect to the one adopted in our previous works.

(1) We do not consider any residual abundance-ratio term in equation (1), i.e. we assume that our solar-scaled correction is able to completely remove (within uncertainties) the combined effect of deviations of single elements from the solar pattern. This choice is motivated by the fact that corrected line strengths are reasonably well fitted, at all radial bins, with solar-scaled models (see Section 5).

(2) In order to account for uncertainties in the absolute calibration of the age (see Section 4.3), we apply an iterative procedure. First, we minimize equation (1) using our reference age estimate for each radial bin (see Section 4.3), then we re-scale *all* age estimates (i.e. for *all* bins) to the median value of the best-fitting $\rm Age_M$ values, and repeat the fitting process. The procedure typically converges after two iterations, with differences between the average Age and $\rm Age_M$ less than a few per cent.

(3) To apply the solar-scaled correction, $C_i(Z_{\rm MW}) \cdot$ [α/Fe], we assume that the slope C_i is a function of metallicity ($Z_{\rm MW}$), rather than velocity dispersion (as in LB13). This choice deserves some clarification. In LB13, we binned SDSS spectra of ETGs with respect to central velocity dispersion, σ, and [α/Fe],[4] resulting into 18 stacks with $100 < \sigma < 300$ km s^{-1}, and a set of seven [α/Fe] substacks at fixed σ. We showed that [α/Fe] provides a good estimate of the deviation of gravity-sensitive features from solar-scaled, in the sense that after removing the *observed* departure of different indices from [α/Fe] = 0 – by means of the index–[α/Fe] correlations at fixed σ – one can fit a variety of features simultaneously with solar-scaled models. In this regard, [α/Fe] should be seen as a metric that measures the deviation of a given spectrum from solar scale, and not only as an estimate of the actual enhancement of α-elements. Because of the [*M*/H]–σ relation in ETGs, metallicity also increases with σ in the LB13 stacks, and thus, the LB13 correction can be applied, in general, either as a function of metallicity or σ. Based on the radial behaviour of gravity-sensitive features analysed in this work (and in particular the Mg4780 indicator, see Appendix A), we argue that a metallicity-driven correction provides the best way to generalize the LB13 approach also to the case of radially binned spectra (where the effects of σ and [*M*/H]are not equivalent, in contrast to SDSS data). In practice, for a given spectrum, we derive the metallicity from the $H\beta_{\rm o}$ versus [MgFe]′ diagram, using MIUSCAT SSP models with a Kroupa-like IMF ($\Gamma_{\rm b} = 1.3$). We calculate the corresponding $C_i(Z_{\rm MW})$ by interpolating the index–[α/Fe] slopes –

[4] In practice, we used the solar-scaled proxy for [α/Fe], see above.

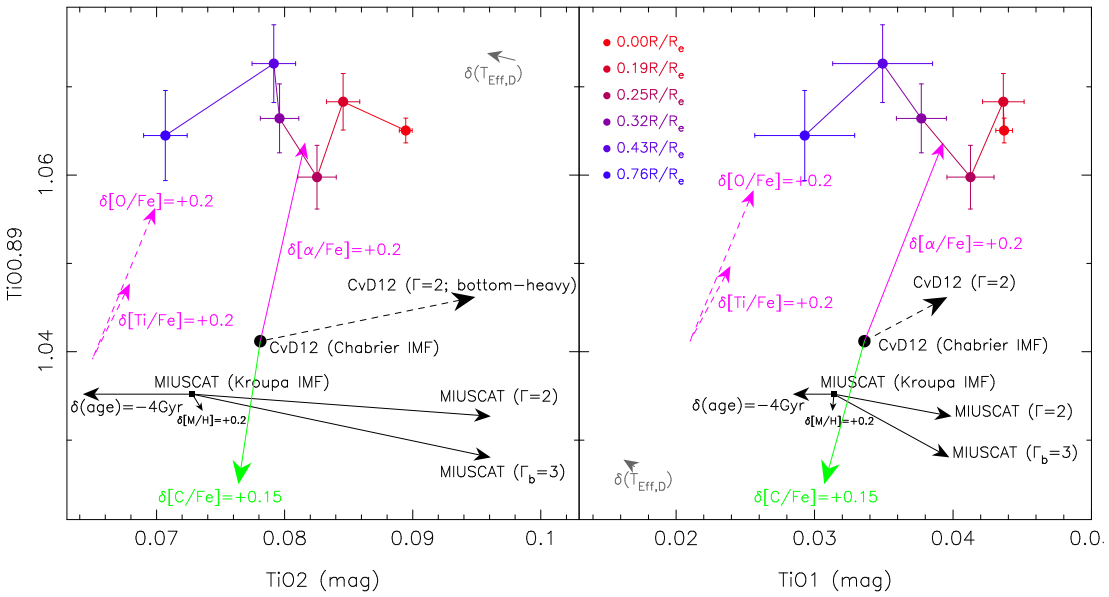

Figure 8. Radial trend of the NIR TiO feature, TiO0.89, as a function of TiO2 (left) and TiO1 (right). Red-through-blue dots, with error bars, correspond to different radial bins, as labelled in the panel on the right. The error bars are quoted at the 1σ level, and include uncertainties on sky subtraction. Solid (dashed) black arrows show the effect of varying the IMF from a Kroupa (Chabrier) to a bottom-heavy IMF, for MIUSCAT (CvD12) SSP models, with an age of 14 (13.5) Gyr and solar metallicity. For both CvD12 and extended-MILES models, we consider bottom-heavy unimodal distributions, with $\Gamma = 2$, while the case of a bimodal bottom-heavy IMF, with $\Gamma_b = 3$, is also shown for the MIUSCAT models. We also show the effect of a change in age and metallicity on the MIUSCAT models, for a Kroupa-like IMF. All TiO features have very little dependence on $[M/H]$, while TiO2 (and to less extent TiO1) decrease with decreasing age. The effect of increasing $[\alpha/Fe]$ ([O/Fe], [Ti/Fe]) by +0.2 dex, in the CvD12 models, is shown by the magenta solid (dashed) arrows, while the green arrows correspond to a variation of +0.15 dex in [C/Fe]. Notice that TiO0.89 is independent of IMF, while it is significantly more sensitive to abundance ratios than TiO2 and TiO1 allowing us to break the degeneracy between abundance ratios and IMF slope. The grey arrows show the effect of changing the temperature of dwarf stars ($\delta(T_{\rm Eff,\,D})$) in the MIUSCAT models (see the text for details). All data and model line strengths refer to a velocity dispersion of 300 km s^{-1} (see Section 4.2).

from the LB13 SDSS stacks – with respect to $Z_{\rm MW}$ (estimated in the same way for the given spectrum and the SDSS stacks). We notice that our approach, where the C_i are a function of $M_{\rm MW}$, is also motivated by the correlation of IMF slope and metallicity, recently found by Martín-Navarro et al. (2015c, hereafter MN15c).

In a forthcoming paper (La Barbera et al., in preparation), we will publish the coefficients $C_i(Z_{\rm MW})$ for all gravity-sensitive features covered by SDSS spectra, providing a detailed description of how one should apply our empirical corrections to galaxy spectra.

5 RESULTS

We start by discussing the radial profiles of IMF-sensitive features in XSG1. In Section 5.1, we focus on the TiO1, TiO2, and TiO0.89 spectral features, as they allow us to disentangle the IMF trends with other population features, such as abundance ratios. The radial behaviour of other IMF-sensitive optical features (i.e. aTiO and Mg4780) is discussed in Appendix A. In Section 5.2, we perform a qualitative comparison of observations and model predictions for the Wing–Ford band. Section 5.3 shows results of our fitting procedure applied to all observed line strengths, i.e. the relation between IMF slope and galactocentric distance in XSG1; Section 5.4 deals with implications for the stellar mass-to-light ratio gradient in XSG1, in comparison with dynamical constraints.

5.1 Radial profiles of optical and NIR TiO features

5.1.1 Disentangling IMF from other effects

Fig. 8 shows one of the main results presented here, namely the radial trends in the TiO0.89 versus TiO2 (left) and TiO0.89 versus TiO1 diagrams (right) for XSG1. In order to perform a qualitative analysis of these trends, the figure also shows predictions of different stellar population models. According to CvD12 models, all three features are sensitive to [C/Fe] and $[\alpha/Fe]$ (see the pink and green solid arrows in the figure), in such a way that the effect of an enhancement in [C/Fe] tends to cancel out an increase in $[\alpha/Fe]$. The sensitivity to $[\alpha/Fe]$ mostly stems from [Ti/Fe] and [O/Fe], as shown by the dashed pink arrows in the figure. However, TiO0.89 is far more sensitive to abundance ratios than TiO1 and TiO2, while it is insensitive to the IMF. In fact, changes of the IMF slope (either unimodal or bimodal) correspond to an almost horizontal shift in both diagrams, as shown by the black solid (MIUSCAT) and dashed (CvD12) lines in the figure. In other words, the effect of abundance ratios and IMF is orthogonal, and thus can be singled out in the plots of TiO0.89 versus both TiO2 and TiO1. The observed line strengths for XSG1 (plotted with red-through-blue circles, moving from the innermost to the outermost bin) show a radial gradient *only for* TiO2 *and* TiO1, while TiO0.89 is almost constant out to the largest radius probed. Notice that the lack of gradient for TiO0.89 is consistent with the competing effect between $[\alpha/Fe]$ and [C/Fe] and the fact that the ratio of $[\alpha/Fe]$ to [C/Fe] is roughly constant with radius in XSG1 (see Section 4.4). The grey arrows in Fig. 8 also show the effect of varying the effective temperature

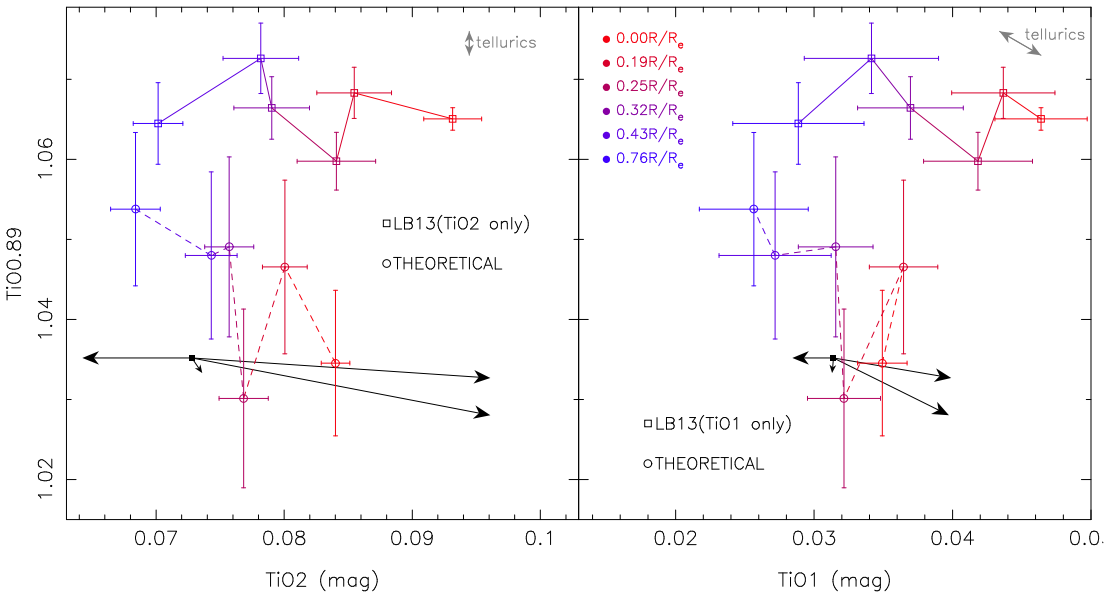

Figure 9. Radial trends of TiO features, as in Fig. 8, but after subtracting off the expected effect of the estimated [α/Fe] and [C/Fe] abundance ratios from each spectral index (only from TiO2 and TiO1 in the LB13 approach, see the labels). Error bars account for the uncertainties on the [α/Fe] and [C/Fe] corrections from different methods (see the text). Notice the fairly good matching of the *theoretically* corrected EWs of TiO0.89 with predictions from MIUSCAT models. The radial gradients of TiO indices are remarkably consistent with a radially varying IMF. Bimodal and unimodal models are fully degenerate in both diagrams, consistent with the results in LB13. Grey arrows show variations in the line strengths of XSG1 from different methods used to remove the telluric lines (see the text). Black arrows are the same MIUSCAT model predictions (with varying age, metallicity, and IMF) as in Fig. 9.

of dwarfs,[5] by adopting the prescription from Pols et al. (1995), cooler than the MIUSCAT reference temperature for dwarf stars (see Vazdekis et al. 2012). Varying $T_{\rm Eff,\,D}$ has a minor effect on both TiO1 and TiO2, and thus cannot explain the observed gradients. Regarding the sensitivity of TiO features to other stellar population properties, we notice that, for [M/H] > -0.4, MIUSCAT models predict both TiO1 and TiO2 to be independent of (total) metallicity (see, e.g., MN15c). For old ages, TiO2 (and to less extent TiO1) tend to decrease with decreasing age, in such a way that a change in age by $\sim$4 Gyr, from an old centre to younger outskirts (solid arrows, labelled δ(age) $= -4$ Gyr), might account for $\sim$1/2 (1/5) of the observed radial gradient of TiO2 (TiO1). In practice, however, XSG1 has no significant radial gradient in age (Section 4.3), and thus a varying IMF is left as the only possible explanation for the TiO0.89 versus TiO2 and TiO1 trends.

As mentioned above (Section 4.5), the use of TiO0.89 in combination with a dwarf-sensitive indicator (e.g. the Wing–Ford band) has been originally proposed by CvD12, to disentangle the effect of giants and dwarfs on the IMF. The present work is the first attempt to combine TiO0.89 and the optical TiO features (in particular, TiO2 and TiO1) to disentangle the effect of the IMF with respect to giant stars *and* abundance ratios. Recently, McConnell et al. (2015) have used TiO0.89 to investigate the origin of radial trends of IMF-sensitive features in two nearby ETGs, with σ = 230 km s^{-1} (NGC 1023) and σ = 245 km s^{-1} (NGC 2974). They found a slightly decreasing radial trend of TiO0.89 for NGC 1023 (with a variation of $\sim$0.01 out to 1 $R_{\rm e}$) and a constant trend for NGC 2974, the latter being consistent with our findings for XSG1.

5.1.2 *Abundance ratios: theoretical predictions*

While there is some difference between solar-scaled CvD12 and MIUSCAT model predictions for TiO features (see the black circle and small black square in Fig. 8), the most remarkable offset in the figure is the one between the TiO0.89 model predictions and the observed points. The observed TiO0.89 is significantly higher (by $\sim$0.03) than in CvD12 and MIUSCAT models. This might be driven by non-solar abundance ratios (i.e. [α/Fe] and [C/Fe]), or some other effects.[6] The effect of abundance ratios is further illustrated in Fig. 9, where we use CvD12 (theoretical) model predictions to remove the expected effect of [α/Fe] and [C/Fe] from all TiO lines (see the open circles in the plot). In practice, for each feature, we estimate the difference of line strengths between the [α/Fe]- ([C/Fe]-) enhanced CvD12 SSP, and the solar-scaled one, for old age (13.5 Gyr), a Chabrier IMF, and the same velocity dispersion as the observed spectrum at a given radial bin. We re-scale these differences to the measured values of [α/Fe] ([C/Fe]) for XSG1. The re-scaled line-strength differences (i.e. the *theoretical abundance corrections*) are subtracted off from the observed values. The error bars account for the statistical errors on line strengths as well as for uncertainties on [C/Fe] and [α/Fe] from different methods (Section 4.4). Remarkably, the theoretically corrected values of TiO0.89

[5] Decreasing the temperature of giants, $T_{\rm Eff,\,G}$, can also (partly) mimic a varying IMF in the TiO1 and TiO2 indices (see MN15a). However, as shown by Spiniello, Trager & Koopmans (2015b), when taking total metallicity into account, the effect of $T_{\rm Eff,\,G}$ is irrelevant to constrain the IMF. Varying $T_{\rm Eff,\,G}$ produces an 'oblique', rather than horizontal (IMF), shift in the TiO0.89 versus TiO2/TiO1 plots, in contrast to the observed (horizontal) trends.

[6] In particular, CvD12 showed that TiO0.89 is strongly sensitive to giant stars (see section 4.3 and fig. 16 of CvD12). As mentioned above, the lack of a gradient in TiO0.89 for XSG1 points to no significant radial change in the properties of giants, but rather a genuine radial variation of the dwarf-to-giant ratio in the IMF.

are fairly consistent with MIUSCAT (and CvD12) solar-scaled predictions. However, one should notice that theoretical corrections are estimated at a specific point in parameter space (i.e. the CvD12 models provide a grid of values for the age, IMF, and metallicity), and might be not exactly the same for. More importantly, theoretical stellar population models rely on ingredients, such as the stellar atmosphere calculations, that carry notoriously difficult uncertainties. Hence, we use theoretical corrections in a qualitative manner throughout the present work, whereas we rely on *empirical abundance corrections* (see also Section 4.5) to perform a quantitative analysis.

5.1.3 Abundance ratios: empirical corrections

Fig. 9 compares the theoretical (circles) and empirical (squares) abundance corrections on TiO1 and TiO2 line strengths. Notice that for TiO0.89 only the theoretical approach is currently possible, as this feature is not covered by the SDSS spectra analysed in our previous works. Therefore, the offset between empirically corrected points (squares) and model predictions (black arrows) for TiO0.89 in Fig. 9 should not be regarded as a discrepancy between models and data, but rather as the effect of abundance ratios that, at present, cannot be described with the LB13 'empirical' approach. Since TiO0.89 is not used in the fitting procedure, the above offset does not affect any of the quantitative estimates regarding IMF variations in XSG1 (Section 5.3). In LB13, we found that TiO1 and TiO2 do not depend much on the abundance ratio at fixed velocity dispersion (metallicity). More precisely, the TiO line strengths are found to increase (decrease) slightly with abundance ratio at the lowest (highest) velocity dispersions (i.e. metallicity, in our refined approach, see Section 4.5, and section 5.2 of LB13). Figs 8 and 9 show that this small dependence on abundance ratio likely arises, *qualitatively*, from the counteracting effect of [α/Fe] and [C/Fe]. As a result, the empirical corrections tend to stretch out the radial variations of TiO1 and TiO2, making the radial gradient of TiO1 (and also TiO2) even more pronounced than in the original, uncorrected data. We add in quadrature the statistical errors of TiO1 and TiO2 to the error budget derived from our empirical correction procedure, giving the error bars shown as the open squares in Fig. 9. Notice that although ideally theoretical and empirical corrections should agree, in practice they do not. The theoretical approach tends to shift both TiO1 and TiO2 towards lower values, in contrast to the empirical one, where the trends are stretched out towards higher values. This might be due to limitations in the theoretical estimates (see above). In addition, a combination of departures of other element abundance ratios such as [Mg/Fe], [Si/Fe] – that individually do not produce a major change in the TiO line strengths – can compensate, along with [C/Fe], the increase in TiO1 and TiO2 due to [O/Fe] and [Ti/Fe]. In practice, when inferring the IMF, the fact that TiO1 and TiO2 are lower when relying on theoretical abundance corrections would be compensated by a younger age in our fitting procedure, implying similar IMF radial trends[7] as those presented in Section 5.3. Since we have not been able to find a consistent interpretation of all the observed indices when relying on theoretical models (see below and Appendix A) and because of the current limitations of the publicly available CvD12 models (see above), our quantitative analysis relies fully on the empirical approach.

[7] In fact, since the sensitivity of the TiO features to the IMF slope is lower in younger populations, the use of either theoretical or empirical corrections would result in similar IMF gradients for XSG1.

5.1.4 Possible issues with data reduction

One might wonder to what extent the trends in Figs 8 and 9 might be driven by an issue related to the data-reduction process. The grey arrows in Fig. 9 show the effect of a change in the telluric correction method in the reduction process (i.e. telluric standard stars versus MOLECFIT, see Section 2) on TiO line strengths. The effect is negligible for TiO0.89 and TiO2, while it is mild for TiO1. Notice that although the spectral region of TiO0.89 is affected by telluric lines, the telluric correction is remarkably accurate (see also Fig. 4), thanks to the excellent quality – especially the high resolution – of our X-shooter data. The telluric correction uncertainty is added in quadrature to the error bars on the empirically corrected line strengths. Other changes in the reduction process (e.g. sky subtraction) have been found not to affect at all the observed TiO line strengths.

5.2 Constraints from the Wing–Ford band

The optical gravity-sensitive spectral features constrain the mass fraction of low-mass stars in the IMF (see LB13), and thus do not allow for different functional forms of the IMF to be singled out. This is illustrated in Fig. 8, where one can see that an increase of the IMF slope of both bimodal and unimodal models produces the same shift in TiO1 and TiO2, and only a tiny difference, with respect to the observed scatter, in TiO0.89. On the other hand, the Wing–Ford band, FeH0.99, is sensitive to very low mass stars in the IMF (see fig. 17 of CvD12). Hence, a combination of this feature with optical indicators allows one to better constrain the functional form of the IMF at the low-mass end, discriminating, for instance, between unimodal and bimodal models.

Fig. 10 shows the abundance-sensitive ([Fe/H]) feature $\langle$Fe$\rangle$ = (Fe5270 + Fe5335)/2, in the optical, as a function of FeH0.99 (see fig. 12 of CvD12a). We show extended-MILES SSP predictions for bimodal (solid black lines) as well as unimodal (green line) models with solar and super-solar metallicities (small and big diamonds, respectively). The extended-MILES predictions are compared to those for CvD12 unimodal models (black dashed line). Both sets of models agree for an MW-like IMF, for which the FeH0.99 line strengths from extended-MILES and CvD12 differ by only $\sim$0.03 Å. However, the change of FeH0.99 with Γ (black dotted for extended-MILES, black dashed line for CvD12 models) is remarkably weaker in extended-MILES with respect to the CvD12 models. Notice that for many IMF-sensitive indicators (e.g. Na- and Ca-dependent features) the response to the IMF is also significantly model-dependent (e.g. LB13; Spiniello et al. 2015b). On the other hand, the behaviour of TiO features seems quite robust between different models (see the solid versus dashed black lines in Fig. 8). Fig. 10 shows that, using the extended-MILES models, FeH0.99 increases with total metallicity (CvD12a models do not vary [M/H]), and increases with the IMF slope more strongly for the unimodal case. The variation of the index is much weaker for a bimodal IMF, where the low-mass end is tapered off by construction. The pink arrows in the figure show the effect of varying [α/Fe] (by +0.2 dex), at fixed [M/H], on both FeH0.99 and $\langle$Fe$\rangle$. The FeH0.99 and $\langle$Fe$\rangle$ variation with [α/Fe] is computed from α-enhanced and solar-scaled CvD12 models (Chabrier IMF, 13.5 Gyr, solar metallicity), removing the effect of the change in total metallicity due to the fact that CvD12 models are computed at fixed [Fe/H] (rather than [M/H]). We remind the reader that, at the moment, we do not have any empirical method to correct the FeH0.99 for abundance variations (see Section 5.1). However, at least for $\langle$Fe$\rangle$, we

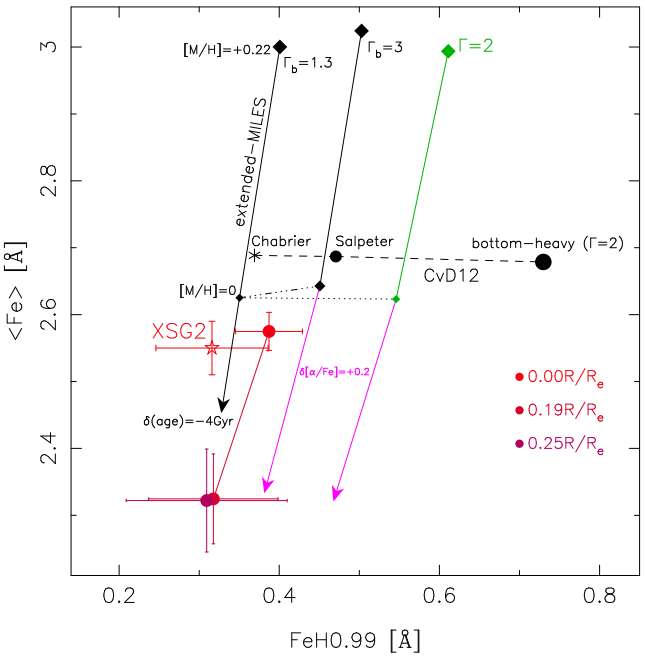

Figure 10. Radial trend of the optical iron indicator, ⟨Fe⟩, as a function of the Wing–Ford band, FeH0.99. Circles with different colours (from red to purple, as labelled) mark different radial bins for XSG1. The open star corresponds to another massive ($\sigma \sim 300$ km s^{-1}; [α/Fe]$\sim$0.25) ETG, XSG2 (see the text). Error bars mark 1σ uncertainties on line strengths. We show predictions for extended-MILES bimodal (solid black lines) and unimodal (solid green line) models with solar and super-solar [M/H] (plotted as small and big diamonds, respectively, for an age of 12.6 Gyr), as well as predictions for CvD12 unimodal models (dashed line), with a Chabrier, Salpeter, and bottom-heavy ($\Gamma = 2$) IMF, at solar metallicity, and an age of 13.5 Gyr. The dotted (dot–dashed) line joins predictions for unimodal (bimodal) extended-MILES models with solar [M/H] (and should be compared with the dashed line for CvD12 models). Both ⟨Fe⟩ and FeH0.99 decrease with increasing [α/Fe], as shown by the pink arrows, for extended-MILES models with Γ_b=3 and $\Gamma = 2$. Notice that the effect of [α/Fe] for $\Gamma_b = 1.3$ (not shown to make the plot more readable) is very similar to the case $\Gamma_b = 3$. All data and model line strengths refer to a velocity dispersion of 300 km s^{-1} (see Section 4.2).

have verified that the predicted effect of [α/Fe] is robust, as the CvD12 model predictions are fairly consistent with those from the α-MILES models. In fact, for δ[α/Fe] = +0.2, we get $\delta\langle$Fe$\rangle \sim -$0.32 Å from CvD12a models (see the pink arrow in the figure for Γ_b = 3), while from α-MILES we get $\delta\langle$Fe$\rangle$ in the range from $-$0.27 to $-$0.35 Å, depending on age, metallicity, and IMF (with the largest variations found in models at the highest [M/H]).

Fig. 10 also shows the observed FeH0.99 for XSG1 as a function of galactocentric distance, with red-through-purple filled circles. Despite of the high S/N ratio of our X-shooter data, the estimates in the outermost radial bins have large uncertainties in FeH0.99 to provide useful constraints on the IMF. Therefore, we focus here on the three innermost radial bins. The most remarkable aspect in the figure is that the observed FeH0.99 is significantly lower than expected for a bottom-heavy unimodal IMF – compare the largest black circle (CvD12 bottom-heavy estimate) with the red dot with error bars (observed data). This mismatch also applies to the extended-MILES models. Specifically, for an old, metal-rich population ($\sim$12.6 Gyr; [M/H]$\sim$+ 0.25 dex), typical values in the central regions of XSG1 (see Fig. 5), and $\Gamma = 2$ (an IMF slope even lower than the one implied by optical IMF-sensitive indicators alone, see Fig. 12), the extended-MILES models give FeH0.99$\sim$0.64 Å (σ = 300 km s^{-1}). For [α/Fe]$\sim$0.4 (see Fig. 7), the FeH0.99 should be lower by $\sim$0.15 Å, implying an expected value of $\sim$0.49 Å in the innermost radial bin, in disagreement with the measured value of FeH0.99 = 0.39 $\pm$ 0.04 Å. Instead, for a bottom-heavy IMF with $\Gamma_b = 3$ (12.6 Gyr, [M/H]$\sim$+ 0.25), the extended-MILES prediction (accounting for [α/Fe]) is FeH0.99$\sim$0.38 Å, fully consistent with the observations. A similar kind of discrepancy with a unimodal IMF is present in the second and third radial bins of XSG1, although it is less significant because of the larger uncertainties on FeH0.99. We emphasize that the sensitivity of FeH0.99 with respect to [α/Fe] is computed in Fig. 10 by use of the CvD12 models for a Chabrier IMF. If such sensitivity were larger for a unimodal bottom-heavy case, relative to a Chabrier IMF, the FeH0.99 might decrease more strongly with [α/Fe] than shown in Fig. 10, making this discrepancy less significant. However, it seems not to be the case. The second massive galaxy, XSG2 (with $\sigma \sim 300$ km s^{-1}), observed as part of the same programme (Section 2), is shown as an open star with error bars in Fig. 10. XSG2 has a *lower* [α/Fe](~0.25) than XSG1, and its FeH0.99 is far too low with respect to the bottom-heavy unimodal predictions. In the following section, we show that a bottom-heavy bimodal IMF matches both optical indicators and the Wing–Ford band in XSG1.

5.3 Radial trends of IMF slope

By use of the method described in Section 4.5, we fit IMF-sensitive features of XSG1 with either unimodal or bimodal extended-MILES SSP models. Fig. 11 shows the fitting results for bimodal models, plotting TiO1, TiO2, aTiO, Mg4780, and FeH0.99 as a function of galactocentric distance. The unimodal fits are not shown in the figure, as the comparison of best-fitting and observed line strengths is very similar to that for bimodal SSPs.

We fit separately (i) the optical indicators and (ii) the Wing–Ford band.

(i) For the optical indices (TiO1, TiO2, aTiO, and Mg4780), we have applied the empirical corrections with respect to abundance pattern, and used our iterative approach to account for the uncertainty on the absolute age zero-point, as described in Section 4.5.

(ii) The fit with FeH0.99 uses simultaneously FeH0.99, Mgb5177, [MgFe]$'$, and ⟨Fe⟩ without any iterative approach, but assuming the age constraint (i.e. the term Age in equation 1) from the fit of optical features (i). Indeed, the age constraints do not affect significantly the results for FeH0.99, as this feature is largely independent of age (see Fig. 11). In the fit for FeH0.99, we do not apply the empirical corrections for abundance pattern, as they are not available for this feature. Instead, we include [α/Fe] as a free-fitting parameter, using FeH0.99, Mgb5177, [MgFe]$'$, and ⟨Fe⟩ to constrain, simultaneously, the parameters [M/H], [α/Fe], and the IMF slope. To this effect, the sensitivity of FeH0.99 to [α/Fe] is modelled, at fixed [M/H], as discussed in Section 5.2. We have found that our results (see below) remain unchanged if (a) we assume our proxy-based estimate of [α/Fe] in each radial bin (Fig. 7), and fit simultaneously only FeH0.99 and [MgFe]$'$ to infer [M/H] and IMF slope (either bimodal or unimodal), and (b) we also fix [M/H] to the output from the step (i), and use FeH0.99 only to infer the IMF slope.

Black symbols and lines in Fig. 11 refer to corrected indices. Uncorrected values are plotted as green lines. All line strengths in the figure are corrected to a common velocity dispersion of 300 km s^{-1} using the best fit from the (bimodal) extended-MILES models (see

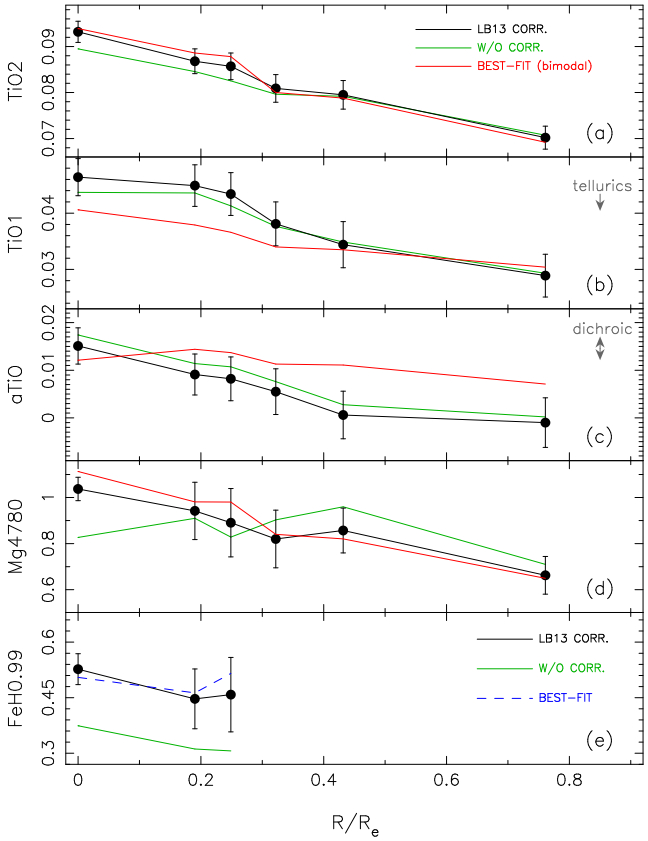

Figure 11. Comparison of observed and best-fitting IMF-sensitive features as a function of galactocentric distance, R/R_e, in XSG1. In panels a, b, c, and d, the observed EWs, empirically corrected to solar scale (see Section 4.5), are plotted in black. The green curves are the uncorrected values, and the bimodal best-fitting line strengths, obtained by simultaneously fitting all the optical indicators (TiO1, TiO2, aTiO, and Mg4780), are shown in red. In panel e (Wing–Ford band), the corrected values are obtained by removing the effect of the best-fitting [α/Fe] from the measured line strengths (see Section 5.2), while the blue line shows extended-MILES (solar-scaled) best-fitting line strengths. Error bars denote 1σ uncertainties, including errors on the correction procedure, as well as the telluric correction (see the grey arrow in panel b) and dichroic continuum variations (see the grey arrows in panel c). All line strengths have been corrected, based on the best-fitting extended-MILES model in each bin, to $\sigma = 300$ km s^{-1} (see Section 4.2).

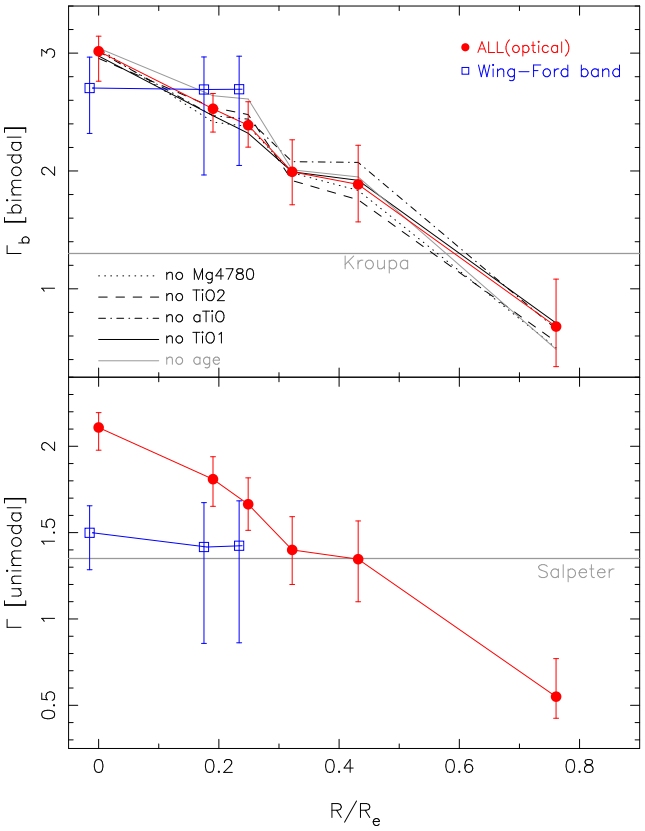

Figure 12. Bimodal (top; Γ_b) and unimodal (bottom; Γ) IMF slope as a function of galactocentric distance for XSG1. Error bars denote 1σ uncertainties. Black lines and symbols correspond to different methods to constrain the slope, using different optical features, as labelled in the top panel. Red curves and symbols show the IMF slopes derived by combining all the optical IMF-sensitive indicators analysed in the present work (i.e. TiO1, TiO2, aTiO, and Mg4780). Blue symbols and curves plot the IMF slope inferred using only the Wing–Ford band. Notice that in this latter case only the three innermost radial bins are plotted, as measurement errors on FeH0.99 do not allow us to obtain significant constraints for the three outermost bins. For a bimodal IMF, we find excellent agreement among optical indicators and FeH0.99, while unimodal IMF slopes, inferred from the FeH0.99, are on average too low (at more than the 3σ level) with respect to the optical constraints. Notice that the inferred radial profile of $\Gamma_b$is consistent when excluding any one index from the analysis (see different line types, in black), as well as when completely neglecting the age constraints in the fitting procedure (grey solid curve; see the text).

Section 4.2). The best-fitting line strengths are shown as red and blue lines in Fig. 11 for the optical and FeH0.99 indices, respectively. The best-fitting values of Γ (unimodal) and Γ_b (bimodal) are shown in the lower and upper panels of Fig. 12, respectively. We also display, with different line types, the results for bimodal models with different combinations of optical indicators. We also show the result when lifting the constraint on the age [grey curve; where the first term in equation (1) is neglected].

Figs 11 and 12 show the main results of the present work, as follows.

(1) All the optical (TiO-based) IMF-sensitive features in XSG1 show a significant radial gradient, implying an IMF gradient in this massive galaxy, from bottom-heavy in the centre to MW-like at $R/R_e \gtrsim 0.5$. Fitting all the optical features simultaneously (red lines in the figures), we measure a radial decrease from $\Gamma_b \sim 3$ ($\Gamma \sim 2.1$) in the centre to $\Gamma_b \sim 0.6$ ($\Gamma \sim 0.5$) at $R/R_e \sim 0.8$. Notice that all TiO features analysed in the present work are insensitive to IMF slope variations when the IMF is top-heavier than Kroupa (i.e. for $\Gamma_b \lesssim 1.3$, or $\Gamma \lesssim 1$; see figs 11 and 18 in LB13). The fact that the lower error bars for the outermost bin in Fig. 12 are relatively small (going, e.g., from $\Gamma \sim 0.55$ to $\sim$0.4 for unimodal models) is only due to the lowest boundary value of IMF slope (Γ and $\Gamma_b = 0.3$) for extended-MILES models. Hence, our results in the outermost radial bin of XSG1 can be considered fully consistent with a Kroupa-like IMF.

(2) For unimodal models, the Wing–Ford band provides inconsistent constraints (i.e. significantly lower Γ) with respect to those from the optical indicators (blue and red dots in lower panel of Fig. 12, respectively). In the innermost radial bin, the Γ derived with FeH0.99 is smaller than the optical-based one by -29 ± 8 per cent, i.e. the discrepancy is significant at more than 3.5σ. In particular, this result seems not to be specific to XSG1, as also for XSG2 – the second galaxy we have observed with X-shooter – the FeH0.99 is far too low to be consistent with a unimodal IMF (see Section 5.2).

(3) For a low-mass tapered bimodal IMF, we get fully consistent results between optical lines and the FeH0.99. In the innermost bin, the difference between FeH0.99- and optical-derived Γ_b is -10 ± 10 per cent.

Regarding the quality of the fits (i.e. Fig. 11), one should notice the following.

(i) The fit using optical features (red curves in the figure) describes remarkably well the TiO2 and Mg4780 observed trends (black circles and lines). We emphasize that the uncorrected line strengths of Mg4780 do not show any clear radial gradient (green curve in panel d). It is our empirical abundance-pattern correction that reveals a radial gradient in this feature, making it fully consistent with TiO2. Notice also that, as discussed in Appendix A, in the innermost bin, the empirical correction is the same when applying it either as a function of velocity dispersion or metallicity. However, in the former, the external corrected values of Mg4780 in panel d would be too high with respect to the best-fitting solution. This is consistent with what we reported in MN15a, where the radial gradient of Mg4780 was found to be too small with respect to that of other features, when applying our empirical approach in terms of velocity dispersion. Our refined method, where abundance-pattern corrections are performed as a function of metallicity, provides consistent results.

(ii) For TiO1, the three innermost data points appear too high (at the $2\,\sigma$ level) with respect to the best fits. This discrepancy might be explained by uncertainties in our telluric correction procedure (see Section 5.1). Using MOLECFIT rather than telluric standard stars in the reduction process (see Section 2), we get systematically lower TiO1, by $\sim$0.003 mag (see the grey arrow in panel b of Fig. 11), making TiO1 more consistent with our best-fitting solution at all radii.

(iii) For aTiO, the best-fitting solution shows a shallow radial gradient. These results from two competing effects: aTiO is expected (from extended-MILES models) to increase with the IMF. However, while the index is independent of metallicity for a Kroupa-like IMF, it *decreases* with [M/H] for a bottom-heavy IMF. Hence, in the inner regions, i.e. towards higher [M/H] and IMF slope, one would not expect large variations in the index. These competing trends, as well as the strong sensitivity of aTiO to the continuum (see Appendix A), make this index, in practice, a less useful IMF indicator than TiO1, TiO2, and also Mg4780. The fact that the observed aTiO shows a gradient, but the best-fitting solution does not, might be due to a combination of uncertainties in the empirical correction of this index, along with issues with the absolute/relative calibration of aTiO because of the instability of the X-shooter dichroic response with time (see Section 2, Appendix A, and grey arrows in panel c of Fig. 11).

(iv) For the Wing–Ford band, we obtain excellent agreement between the observed and best-fitting line strengths (blue and black lines in panel e of the figure), although such a result is to be expected, considering that, in this case, the only IMF-sensitive feature used in the fitting procedure is FeH0.99. As mentioned above, the remarkable result is that one gets very consistent constraints, for a *bimodal* IMF, between the optical features and the Wing–Ford band.

Finally, we want to emphasize that, although there are a few discrepancies between the observed and best-fitting optical indicators in some radial bins (i.e. TiO1 in the three innermost, and aTiO in the two outermost bins), Fig. 12 shows that the quality of the fit is good, within error bars. Moreover, the inferred radial profile of the bimodal IMF slope, Γ_b, is consistent when excluding any one index from the analysis (see different line types in the figure), i.e. if we include in the fitting, for each bin, only those indices for which models give a better matching to the data. This proves that our results are robust, and not affected by possible mismatches between data and models. We also emphasize that *when completely neglecting the age constraints* in the fitting procedure, we get very consistent results to our reference IMF profile (solid red curve) in Fig. 12, implying that our findings are not affected by the uncertainty on the absolute age zero-point.

5.4 Constraints on the normalization of the IMF

The radial trend of IMF slope found in XSG1 (Fig. 12) leads to a radial gradient in the stellar mass-to-light ratio, $M_\star/L$. To quantify it, we use the mismatch parameter $\alpha \equiv (M_\star/L)/(M_\star/L)_{\rm MW}$, defined as the ratio between the stellar M/L corresponding to the best-fitting age, metallicity, and IMF slope, and the one derived for the same age and metallicity, assuming an MW-like IMF (we adopt as MW reference a bimodal $\Gamma_b = 1.3$ IMF). We derive α as a function of galactocentric distance. Notice that for an MW-like normalization, $\alpha \sim 1$, whereas either bottom- or top-heavy IMF gives $\alpha > 1$ because of the higher fraction of low-mass stars, or remnants, respectively. A Salpeter normalization implies $\alpha \sim 1.6$. At each radius, we compute $M_\star/L$ from bimodal IMF models, as unimodal models are inconsistent with constraints from optical features and the Wing–Ford band. To this effect, we random shift the values of Γ_b, from the best-fitting estimate at the given radius (Fig. 12), according to their uncertainties, and compute the average $M_\star/L$ and its error. The computation excludes top-heavy models with $\Gamma_b < 0.5$, as these models have $M_\star/L$ much larger than the MW reference ($\Gamma_b \sim 1.3$), but they are indistinguishable, concerning our IMF-sensitive indicators, from the case with $\Gamma_b \sim 1.3$. Fig. 13 plots α as a function of galactocentric distance (black circles, with 1σ error bars). As expected from the radial trend of Γ_b, the α parameter also decreases with R/R_e, from $\sim$2 in the innermost radial bin to $\sim$1 beyond half of the effective radius. The red curve in the figure shows the integrated constraints on α, i.e. the luminosity-weighted values of α computed within concentric circular apertures, under the assumption of circular symmetry. As expected, the integrated version of α shows a slower decline with radius, with respect to the local one, becoming slightly lower than the Salpeter value already within $R_e/2$ (second outermost red point, and dashed horizontal line). Fig. 13 also shows as a blue square the mismatch parameter, $\alpha_{\rm JAM}$, obtained by normalizing the total mass-to-light ratio from the JAM (Section 4.1) to the stellar M/L for a Kroupa-like IMF (see above). Notice that we find $(M/L)_{\rm JAM} = 7.5 \pm 0.75$, implying $\alpha_{\rm JAM} = 1.83 \sim 0.17$. $(M/L)_{\rm JAM}$ can be interpreted as the ratio between total mass (including dark matter, which is likely $\lesssim$30 per cent within the central galaxy regions; see Cappellari et al. 2013a) and the r-band luminosity within a sphere of radius $R\sim$2 arcsec. This is actually the region where the data are more reliable and the fit using JAM describes them better. For $R\sim$2 arcsec ($R/R_e \sim 0.5$), our bimodal IMF fits imply an aperture integrated value (see the red circles in the figure) of $\alpha \sim 1.57$, i.e. smaller than $\alpha_{\rm JAM}$. Hence, not only our spectroscopic constraints are consistent between optical and NIR indicators, but they are also consistent with the dynamical analysis. The ratio $(\alpha_{\rm JAM} - \alpha)/\alpha_{\rm JAM}$ gives the dark-matter fraction (i.e. the ratio of non-stellar to total mass) for XSG1, within half the effective radius, and amounts to 14 ± 11 per cent, consistent with the expectation that this galaxy

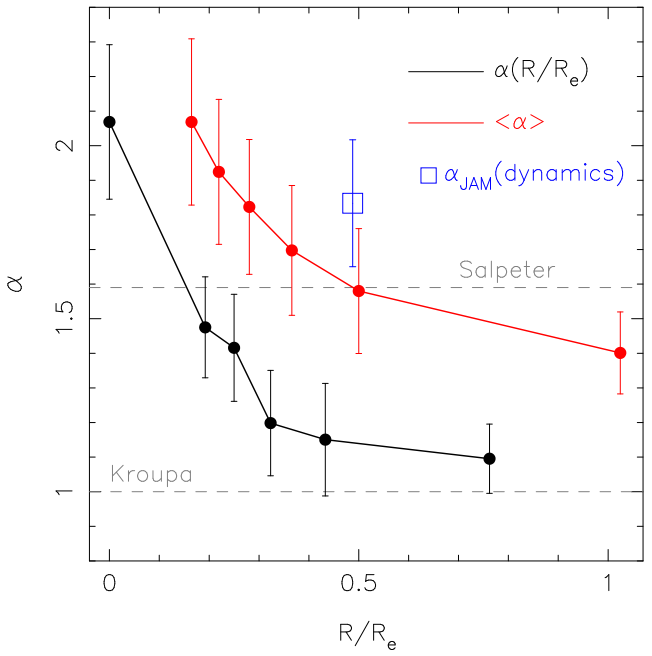

Figure 13. Radial trend of the IMF mismatch parameter, α, for bimodal IMF models (see the text for details). The black line and symbols show the local values of α, while the luminosity-weighted value, $\langle\alpha\rangle$, measured over circular apertures, is plotted in red. Error bars denote 1σ level uncertainties. The blue square plots the mismatch parameter, $\alpha_{\rm JAM}$, obtained from the JAM dynamical analysis (Section 4.1). Notice that unimodal models would produce an overly high $\langle\alpha\rangle$ ($\sim$3) with respect to $\alpha_{\rm JAM}$.

should have a minor dark-matter contribution in the central region (Cappellari et al. 2015; Posacki et al. 2015).

6 DISCUSSION

6.1 IMF gradients in ETGs

The existence of a radial gradient of the IMF in XSG1 agrees well with our previous results for NGC 4552 and NGC 5557 – two massive nearby ETGs with central velocity dispersion of 280 and 300 km s^{-1}, respectively (MN15a). For NGC 4552 (the best target in MN15a), the bimodal IMF slope decreases from $\Gamma_{\rm b} \sim 3$ in the galaxy centre to $\sim$2 at $R \sim 0.4R_{\rm e}$, consistent with the profile in Fig. 12 for XSG1. Notice, however, that the velocity dispersion profile of XSG1 ranges from $\sim$340 km s^{-1} in the centre to $\sim$270 km s^{-1} at $R_{\rm e}$. Hence, our results extend the findings of MN15a at significantly higher velocity dispersion, suggesting that IMF gradients are common in high velocity dispersion ETGs. On the other hand, we do not expect such gradients to be universal. In Martín-Navarro et al. (2015b, hereafter MN15b), we derived the IMF profile of the massive and compact 'relic' galaxy NGC 1277 ($\sigma \sim 400$ km s^{-1}), finding only a mild IMF gradient, with $\Gamma_{\rm b}$ decreasing from $\sim$3 in the galaxy centre to $\sim 2.5 \pm 0.4$ at $R/R_{\rm e} \sim 1$. In MN15c, analysing a sample of ETGs from the Calar Alto Legacy Integral Field Area Survey (CALIFA) (with $160 \lesssim \sigma \lesssim 280$ km s^{-1}) we found that locally – i.e. at a given position within the galaxy – $\Gamma_{\rm b}$ is best correlated with total metallicity. Remarkably, no radial variation is found in any of the observed properties of XSG1 (e.g. kinematics profile, stellar population properties, abundance ratios), except for IMF and metallicity, reinforcing the idea of a tight connection between these two parameters. Similarly to NGC 1277, XSG1 has a high σ, and very high abundance ratios ([α/Fe]$\sim+$ 0.4; comparable to NGC 1277, with [α/Fe]$\sim+$ 0.3), with no age gradient and no radial variation of [α/Fe] within $R_{\rm e}/2$ (see Fig. 7). Nevertheless, XSG1 and NGC 1277 have very different radial variations of the IMF, suggesting that one may expect, in general, a wide range of IMF profiles in massive ETGs. This variety, also expected from the scatter of the IMF–[M/H] relation (see MN15c), is similar to the observed metallicity gradients in ETGs. On average, a correlation of [M/H] gradients with velocity dispersion is detected (see, e.g., La Barbera et al. 2010a). However, this correlation is tighter at low velocity dispersion ($\sigma < 150$ km s^{-1}), whereas a wide scatter of metallicity gradients is observed in more massive ETGs (see, e.g., fig. 8 of Spolaor et al. 2010), ranging from almost null to significantly negative (δ[M/H]/$\delta \log R \sim -0.6$). This scatter originates possibly from the different merging histories of massive ETGs (Hopkins et al. 2009). Our results for XSG1 and other massive galaxies suggest that each specific channel of ETG formation will shape the radial IMF profile of ETGs. While an IMF gradient will be produced by the different star formation and chemical enrichment processes at different radii during the initial stages – likely through a time-varying IMF scenario (Weidner et al. 2013; Ferreras et al. 2015) – this gradient is expected to be modified at later times through the different merging events. This scenario naturally yields a range of IMF radial gradients in nearby ETGs, possibly without a sharp correlation with any specific property of the galaxy.

While in our previous works (MN15a and MN15b) we presented evidence against abundance ratios and other systematic effects, such as the effective temperature of giants/dwarfs, as the major driver of radial gradients of IMF-sensitive features in ETGs, we separate more explicitly in XSG1 the effect of the IMF from other confounding factors. We find a significant radial gradient of features sensitive to the dwarf-to-giant ratio in the IMF (e.g. TiO1 and TiO2), whereas no gradient is detected either in the abundance ratios ([α/Fe]; [C/Fe]) or TiO0.89, sensitive to giants and abundance effects, but insensitive to dwarfs). To our knowledge, this is the clearest evidence so far of a radial IMF gradient in a massive galaxy. The combination of no gradient in [α/Fe] and a radial trend in the IMF confirms our previous claim that abundance-ratio variations cannot be the major driver of the observed trends (LB13). These results are in good agreement with the relation between dynamically determined IMF mass normalization factors and stellar population parameters (McDermid et al. 2014; Smith 2014). Notice that a better correlation of the IMF with [α/Fe], rather than velocity dispersion, has been originally suggested by Conroy & van Dokkum (2012b), but it is not confirmed from studies where the effects of σ and [α/Fe] are singled out. Indeed, the correlation of IMF with [α/Fe] in Conroy & van Dokkum (2012b) might be driven by the fact that CvD12 models are computed at fixed [Fe/H], rather than total metallicity.

Recently, McConnell et al. (2015) investigated the origin of radial trends of IMF-sensitive features in two nearby ETGs, with $\sigma = 230$ km s^{-1} (NGC 1023) and $\sigma = 245$ km s^{-1} (NGC 2974), respectively. They detected a radial gradient in the dwarf-sensitive feature Na I8190 ($\lambda \sim 8180$–8200 Å), with only a mild variation of FeH0.99, favouring abundance-ratio variations (in particular, [Na/Fe] and [N/Fe]) as the main explanation for the observed trends of IMF-sensitive features in ETGs. Although the radial behaviour of the IMF might be flat in some massive ETGs (see above), we emphasize that, in practice, the presence of abundance and IMF gradients can coexist, hampering a direct interpretation of the indices. One example is the Mg4780 feature (bTiO; see Spiniello et al. 2014). No significant – at most a very shallow – gradient is observed

for this IMF-sensitive feature for XSG1 as well as NGC 4552 (see MN15a). However, note that abundance ratios tend to wash out the underlying IMF trend, and it is only by correcting for abundance effects that one recovers consistent results with other features (see Appendix A). For some features, like FeH0.99, the interpretation is even trickier. According to predictions from new NIR (extended-MILES) stellar population models with varying total metallicity *and* IMF, the FeH0.99 response to (total) metallicity – and thus also to [α/Fe] at fixed [M/H] – is larger at higher metallicity. Hence, even if [α/Fe] were constant (as in XSG1), the [α/Fe] tends to further decrease the observed line strength of FeH0.99 in the galaxy centre with respect to the outer regions, counteracting the effect of a steeper IMF in the centre (i.e. reducing the radial gradient of FeH0.99). Notice that in LB13 we also reported that the abundance-ratio response of some gravity-sensitive features might be coupled with the IMF slope. For instance, in LB13 (see fig. 15) the response of Na I8200 (CaT) to [Na/Fe] ([Ca/Fe]) was shown to be likely stronger (weaker) for SSP models with a bottom-heavy IMF, relative to Kroupa. This coupling, not included in any publicly available version of stellar population models with varying abundance ratios (e.g. CvD12), might be responsible for some of the apparent contradictions between model predictions and observations (Smith et al. 2015b).

6.2 IMF shape and mass-to-light ratio gradients in ETGs

Our analysis of optical and NIR features in XSG1 is inconsistent with a unimodal, single power-law IMF, favouring a functional form tapered off at the low-mass end, such as the bimodal IMF of Vazdekis et al. (1996). We emphasize that this result does not imply that the IMF functional form has to be bimodal. As discussed in FER13 and LB13, unimodal IMF models are also disfavoured by the fact that they predict overly high stellar M/L ratios with respect to simple dynamical constraints. However, a possible way out is to assume a unimodal parametrization, increasing the low-mass-end cutoff, $M_{\rm low}$, in the IMF (with $M_{\rm low} \lesssim 0.15$ M$_\odot$; see Barnabé et al. 2013; Spiniello et al. 2015b). In fact, very low mass stars (< 0.15 M$_\odot$) do not contribute significantly to the integrated galaxy light, while they provide a major contribution to the M/L. Since the Wing–Ford band is sensitive to the very low mass stars in the IMF (see Fig. 17 of CvD12), increasing $M_{\rm low}$ might also reconcile optical and NIR indicators for XSG1, in the same way as adopting a bimodal IMF. However, this option is rather contrived, and would beg the question of why such a gap exists between low-mass stars and massive brown dwarves. An alternative approach, taken by Conroy & van Dokkum (2012b), is to assume a three-segment set of power laws for the IMF, describing individually the behaviour of very low, and low, mass stars. In this parametrization, our results for XSG1 would imply that the IMF has to be steep at low, but not at very low mass. While the information on the detailed shape of the IMF is imprinted in the optical and NIR features of a galaxy spectrum (CvD12), it is not clear if this information can be recovered, mostly because of current uncertainties on stellar population models, and on modelling the effect of variations in the abundance ratios on the targeted spectral features. Regardless of the detailed shape of the IMF, one important result from the present work is that spectroscopic constraints are inconsistent with a pure unimodal parametrization of the IMF extended down to the H-core burning stellar mass limit. We notice that our dynamical analysis, based on JAM modelling with an approach as close as possible to that of the ATLAS^{3D} sample, provides M/L constraints fully consistent with our stellar population analysis.

Recently, Smith, Lucey & Conroy (2015a, hereafter SLC15) analysed a sample of nearby ETGs where M/L can be constrained through strong gravitational lensing in the inner regions of galaxies. For three systems, SLC15 estimated a 'mass excess factor', α, only marginally consistent with a Salpeter-IMF normalization ($\alpha \sim 1.6$), in tension with stellar population models. Among the three lensing galaxies of SLC15, the more similar one to XSG1 is perhaps SNL-2, with a velocity dispersion of 320 ± 18 km s^{-1}, [α/Fe] $= +0.38 \pm 0.06$, and an effective radius of $\sim$6 kpc (in the J band). Within the Einstein radius ($R_{\rm Ein}$), which probes a region $\sim 0.4\,R_{\rm e}$ for SNL-2, SLC15 derive $\alpha = 1.27 \pm 0.20$ ($\alpha = 0.94 \pm 0.17$), for the case where no dark matter (dark matter) is assumed. At a galactocentric distance of $0.4\,R_{\rm e}$, XSG1 has an (aperture-)integrated value of $\alpha = 1.7 \pm 0.2$, for a bimodal IMF. This value is only marginally higher (below the 1.5σ level) with respect to the no-dark-matter estimate of SLC15. Moreover, as discussed above, one may expect, and we do observe, a variety of IMF profiles in ETGs. Hence, we cannot exclude that the IMF normalization is different when comparing different galaxies (e.g. XSG1 and SNL-2). Furthermore, the estimate of the mass excess, α, changes when adopting different IMF parametrizations in the stellar population analysis (see FER13 and LB13). The case of SNL-1 in SCL15 is also interesting. This lensing galaxy has 356 ± 18 km s^{-1}, [α/Fe] $= +0.31 \pm 0.05$, and an effective radius of $\sim$2 kpc, being more compact than both XSG1 and SNL-2. Within an $R_{\rm Ein}$ of $1.2\,R_{\rm e}$, SLC15 find $\alpha = 1.42 \pm 0.15$ ($\alpha = 1.20 \pm 0.13$), for the case with no-dark-matter (dark-matter). In the case of XSG1, at the maximum galactocentric distance probed of $\sim 1\,R_{\rm e}$, we find an (aperture-)integrated mass excess $\alpha = 1.40 \pm 0.12$ (see the red curve in Fig. 13), fully consistent with the estimate of SLC15 for SNL-1. These comparisons show that radial IMF, and mass-to-light, gradients are an important ingredient when comparing constraints from different techniques.

Spiniello et al. (2015b, hereafter STK15) have recently suggested an anticorrelation between IMF slope and surface density, defined as $\rho = \sigma^2/R_{\rm e}^2$ in units of 1000 (km s^{-1})^2/kpc^2. Since ETGs with high [α/Fe] are also the more compact ones around the Fundamental Plane relation (Gargiulo et al. 2009), the result of STK15 seems consistent with our findings (see LB13), namely, at fixed velocity dispersion, the ETGs with the highest [α/Fe] might also have the lower IMF slopes. However, our preliminary results for XSG2, the second galaxy observed in our X-shooter campaign, challenge this scenario. XSG1 and XSG2 have $\rho \sim 5.5$ and $\sim$2, respectively, i.e. XSG2 is significantly less dense than XSG1. Nevertheless, it has a lower FeH0.99 (see Fig. 10). This result, combined with its higher central metallicity ([M/H] $\sim +0.35$) and lower [α/Fe] ($\sim +0.25$) with respect to the values for XSG1 ([M/H]$\sim +0.25$ and [α/Fe]$\sim +0.4$), implies a lower IMF slope. Moreover, Conroy et al. (2013) found a mismatch parameter $\alpha = 2.27 \pm 0.16$ for stacked spectra of compact ETGs in the SDSS, at $\sigma \sim 270$ km s^{-1}, implying a higher IMF normalization in more compact galaxies with respect to the general population of ETGs (see, e.g., fig. 5 of CvD12b). We point out that the presence of a variety of IMF gradients in massive ETGs complicates the comparison of IMF slopes among galaxies with different degree of compactness. Larger samples are required to address this issue in detail.

7 SUMMARY

We present a detailed analysis of a set of targeted IMF-sensitive line strengths in a massive ($\sigma \sim 300$ km s^{-1}) ETG (XSG1), at $z \sim 0.05$, observed with the VLT/X-shooter instrument. The lack of a significant gradient in the age and [α/Fe] – two stellar population

properties – out to one half of the effective radius (Figs 5 and 7), makes this target especially suited to the analysis of radial variations in the IMF. By combining several TiO-based indices in the optical and NIR, we exploit the different sensitivities to the underlying stellar population parameters to disentangle the contribution from the stellar IMF. The observed indices for XSG1 on the TiO0.89 versus optical TiO diagrams (Fig. 8) show a significant gradient in the optical indices, not followed by the NIR index, which is insensitive to the IMF.

Our findings strengthen the case for radial variations within an effective radius of the IMF in massive ETGs, further supporting the idea (MN15a) that the IMF is a local property of ETGs. In XSG1, we find a bottom-heavy population ($\Gamma_b \sim 3$) in the innermost regions, gradually changing to a standard Kroupa-like IMF ($\Gamma_b = 1.3$) at $R \gtrsim R_e/2$ (Fig. 12). The lack of a measurable gradient in abundance ratios, over the spatial scale where the IMF is found to vary, points to a possible relationship between IMF and total metallicity in regions with high velocity dispersion, in agreement with MN15c.

In addition, we include in the analysis the FeH-based Wing–Ford band, sensitive to very low mass stars. A remarkable mismatch is found when adopting an IMF with a unimodal (single power law) functional dependence. In contrast, a bimodal IMF (which substitutes the power law at the low-mass end with a constant value) is fully consistent with all indicators (Fig. 10). Hence, for the first time, we are able to rule out the unimodal IMF based on a pure stellar population analysis (i.e. beyond the fact that the unimodal stellar M/L is overly high with respect to dynamical constraints; see LB13).

Remarkably, the dynamical analysis based on the JAM of Cappellari (2008) gives a very consistent stellar M/L with respect to the (bimodal) model predictions of the spectroscopic method via gravity-sensitive spectral features (Fig. 13).

From a more technical point of view, the present work generalizes the empirical approach of LB13 to deal with spectra at different galactocentric distances. Remarkably, once *empirical solar-scaled corrections* are applied as a function of total metallicity (rather than velocity dispersion; see LB13; MN15a), we are able to describe fairly well a variety of gravity-sensitive features, including those for which a radial gradient is apparently not detected (Mg4780).

In a future work, we plan to extend the present analysis, by combining TiO- and FeH0.99- based results with constraints from Ca and Na features, to discuss how abundance ratios affect the combined use of these features to constrain the stellar IMF.

ACKNOWLEDGEMENTS

This work is based on observations made with ESO Telescopes at the Paranal Observatory under programmes ID 092.B-0378 and 094.B-0747 (PI: FLB). FLB acknowledges the Instituto de Astrofísica de Canarias for the kind hospitality while this paper was in progress. We thank Dr J. Alcalá for the insightful discussions and help with the reduction of X-shooter spectra. We also thank the anonymous referee for his/her useful comments that helped us to improve our manuscript. We have made extensive use of the SDSS data base (http://www.sdss.org/collaboration/credits.html). MC acknowledges support from a Royal Society University Research Fellowship. We acknowledge support from grant AYA2013-48226-C3-1-P from the Spanish Ministry of Economy and Competitiveness (MINECO).

REFERENCES

Auger M. W., Treu T., Bolton A. S., Gavazzi R., Koopmans L. V. E., Marshall P. J., Moustakas L. A., Burles S., 2010, ApJ, 724, 511
Barnabé M., Spiniello C., Koopmans L. V. E., Trager S. C., Czoske O., Treu T., 2013, MNRAS, 436, 253
Cappellari M., 2002, MNRAS, 333, 400
Cappellari M., 2008, MNRAS, 390, 71
Cappellari M., Emsellem E., 2004, PASP, 116, 138
Cappellari M. et al., 2007, MNRAS, 379, 418
Cappellari M. et al., 2012, Nature, 484, 485
Cappellari M. et al., 2013a, MNRAS, 432, 1709
Cappellari M. et al., 2013b, MNRAS, 432, 1862
Cappellari M. et al., 2015, ApJ, 804, 21
Cenarro A. J., Gorgas J., Vazdekis A., Cardiel N., Peletier R. F., 2003, MNRAS, 339, L12
Cervantes J. L., Vazdekis A., 2009, MNAS, 392, 691
Conroy C., van Dokkum P., 2012a, ApJ, 747, 69 (CvD12)
Conroy C., van Dokkum P., 2012b, ApJ, 760, 71
Conroy C., Dutton A. A., Graves G. J., Mendel J. T., van Dokkum P. G., 2013, ApJ, 776, 26
Dutton A. A., Macciò A. V., Mendel J. T., Simard L., 2013, MNRAS, 432, 2496
Emsellem E., Monnet G., Bacon R., 1994, A&A, 285, 723
Falcón-Barroso J., Sánchez-Blázquez P., Vazdekis A., Ricciardelli E., Cardiel N., Cenarro A. J., Gorgas J., Peletier R. F., 2011, A&A, 532, 95
Ferreras I., Leier D., Saha P., Courbin F., Falco E. E., 2010, MNRAS, 409, L30
Ferreras I., La Barbera F., de la Rosa I. G., Vazdekis A., de Carvalho R. R., Falcón-Barroso J., Ricciardelli E., 2013, MNRAS, 429, L15 (FER13)
Ferreras I., Weidner C., Vazdekis A., La Barbera F., 2015, MNRAS, 448, L82
Gargiulo A. et al., 2009, MNRAS, 397, 75
Hopkins P. F., 2013, MNRAS, 433, 170
Jeong H., Yi S. K., Kyeong J., Sarzi M., Sung E.-C., Oh K., 2013, ApJS, 208, 7
Kausch W. et al., 2015, A&A, 576, 78
Kormendy J., Ho L. C., 2013, ARA&A, 51, 511
La Barbera F., de Carvalho R. R., Kohl-Moreira J. L., Gal R. R., Soares-Santos M., Capaccioli M., Santos R., Sant'anna N., 2008, PASP, 120, 681
La Barbera F., de Carvalho R. R., de la Rosa I. G., Gal R. R., Swindle R., Lopes P. A. A., 2010a, AJ, 140, 1528
La Barbera F., de Carvalho R. R., de la Rosa I. G., Lopes P. A. A., Kohl-Moreira J. L., Capelato H. V., 2010b, MNRAS, 408, 1313
La Barbera F., Ferreras I., Vazdekis A., de la Rosa I. G., de Carvalho R. R., Trevisan M., Falcón-Barroso J., Ricciardelli E., 2013, MNRAS, 433, 3017 (LB13)
La Barbera F., Ferreras I., Vazdekis A., 2015, MNRAS, 449, L137
Lee H., Worthey G., Blakeslee J. P., 2010, ApJ, 710, 421
McConnell N. J., Lu J. R., Mann A. W., 2015, ApJ, preprint (arXiv:1506.07880)
McDermid R. M. et al., 2014, ApJ, 792, L37
Martín-Navarro I., La Barbera F., Vazdekis A., Falcón-Barroso J., Ferreras I., 2015a, MNRAS, 447, 1033 (MN15a)
Martín-Navarro I., La Barbera F., Vazdekis A., Ferré-Mateu A., Trujillo I., Beasley M. A., 2015b, MNRAS, 451, 1081 (MN15b)
Martín-Navarro I. et al., 2015c, ApJ, 806, L31 (MN15c)
Modigliani A. et al., 2010, Proc. SPIE, 7737, 773728
Navarro J. F., Frenk C. S., White S. D. M., 1996, ApJ, 462, 563
Noll S., Kausch W., Kimeswenger S., Barden M., Jones A. M., Modigliani A., Szyszka C., Taylor J., 2014, A&A, 567, 25
Pastorello V., Forbes D. A., Foster C., Brodie J. P., Usher C., Romanowsky A. J., Strader J., Arnold J. A., 2014, MNRAS, 442, 1003
Pols O. R., Tout C. A., Eggleton P. P., Han Z., 1995, MNRAS, 274, 964
Posacki S., Cappellari M., Treu T., Pellegrini S., Ciotti L., 2015, MNRAS, 446, 493

Ricciardelli E., Vazdekis A., Cenarro A. J., Falcón-Barroso J., 2012, MNRAS, 424, 172
Röck B., Vazdekis A., Peletier R. F., Knapen J. H., Falcón-Barroso J., 2015, MNRAS, 449, 2853
Salpeter E. E., 1955, ApJ, 121, 161
Sánchez-Blázquez P., Forbes D. A., Strader J., Brodie J., Proctor R., 2007, MNRAS, 377, 759
Schiavon R. P., Faber S. M., Rose J. A., Castilho B. V., 2002, ApJ, 580, 873
Schönebeck F., Puzia T. H., Pasquali A., Grebel E. K., Kissler-Patig M., Kuntschner H., Lyubenova M., Perina S., 2014, A&A, 572, 13
Serven J., Worthey G., Briley M. M., 2005, ApJ, 627, 754
Smette A. et al., 2015, A&A, 576, A77
Smith R., 2014, MNRAS, 443, 69
Smith R., Lucey J. R., 2013, MNRAS, 434, 1964
Smith R. J., Lucey J. R., Conroy C., 2015a, MNRAS, 449, 3441 (SLC15)
Smith R. J., Alton P., Lucey J. R., Conroy C., Carter D., 2015b, MNRAS, 454, L71
Spiniello C., Trager S., Koopmans L. V. E., Conroy C., 2014, MNRAS, 438, 1483 (STK14)
Spiniello C., Barnabé M., Koopmans L. V. E., Trager S. C., 2015a, MNRAS, 452, L21
Spiniello C., Trager S., Koopmans L. V. E., 2015b, ApJ, 803, 87 (STK15)
Spolaor M., Kobayashi C., Forbes D. A., Couch W. J., Hau G. K. T., 2010, MNRAS, 408, 272
Thomas D., Maraston C., Bender R., 2003, MNRAS, 339, 897
Thomas D., Maraston C., Johansson J., 2011, MNRAS, 412, 2183 (TMJ11)
Tortora C., Romanowsky A. J., Napolitano N., 2013, ApJ, 765, 8
Trager S. C., Worthey G., Faber S. M., Burstein D., González J. J., 1998, ApJS, 116, 1
Treu T., Auger M. W., Koopmans L. V. E., Gavazzi R., Marshall P. J., Bolton A. S., 2010, ApJ, 709, 1195
Tripicco M. J., Bell R. A., 1995, AJ, 110, 3035
van Dokkum P. G., Conroy C., 2010, Nature, 468, 940
Vazdekis A., Arimoto N., 1999, ApJ, 525, 144
Vazdekis A., Casuso E., Peletier R. F., Beckman J. E., 1996, ApJS, 106, 307
Vazdekis A., Salaris M., Arimoto N., Rose J. A., 2001, ApJ, 551, 127
Vazdekis A., Cenarro A. J., Gorgas J., Cardiel N., Peletier R. F., 2003, MNRAS, 340, 1317
Vazdekis A., Ricciardelli E., Cenarro A. J., Rivero-González J. G., Díaz-Garcá L. A., Falcón-Barroso J., 2012, MNRAS, 424, 157
Vazdekis A. et al., 2015, MNRAS, 449, 1177 (VAZ15)
Vernet J. et al., 2011, A&A, 536, A105
Weidner C., Ferreras I., Vazdekis A., La Barbera F., 2013, MNRAS, 435, 2274
Yamada Y., Arimoto N., Vazdekis A., Peletier R. F., 2006, ApJ, 637, 200
Zieleniewski S., Houghton R. C. W., Thatte N., Davies R. L., 2015, MNRAS, 452, 597

APPENDIX A: RADIAL TRENDS OF THE ATIO AND MG4780 IMF-SENSITIVE FEATURES

In addition to the TiO1 and TiO2 indices, we also consider the aTiO and Mg4780 optical features to constrain the IMF in XSG1 (Section 4.5). In this appendix, we describe the radial behaviour of these features.

A1 The aTiOindex

Fig. A1 shows TiO0.89 (see Section 5.1), as a function of aTiO, at different galactocentric distances (red through blue, from the centre outwards). aTiO increases with IMF slope, slightly more in the bimodal case, in contrast to TiO1 and TiO2, for which the line strengths of models with $\Gamma = 2$ correspond exactly to those for $\Gamma_b = 3$ (see Fig. 8). The index is independent of age (see Spiniello et al. 2014), while it is anticorrelated with metallicity. As shown in Fig. A1, the dependence on $[M/H]$ is rather complex, as it is coupled with the IMF. aTiO decreases slightly with $[M/H]$ for an MW-like IMF, while it strongly decreases with $[M/H]$ for a bottom-heavy distribution (see the two black arrows in the figure, for $\delta[M/H] = +0.2$). In other words, aTiO is, *in general*, not a good IMF-sensitive indicator, as at high metallicity it is expected to have essentially the same value for either an MW-like or a bottom-heavy IMF. Hence, for a galaxy with a bottom-heavier IMF in the centre, with respect to the outer regions – as is the case for XSG1 – one would expect a shallow radial gradient in aTiO. In contrast, Fig. A1 shows a significant radial variation of aTiO in XSG1. Using CvD12 models, we find that in addition to the anticorrelation with [Fe/H] (consistent with the one with $[M/H]$ in the MIUSCAT models), aTiO also depends on $[\alpha/Fe]$ and [C/Fe]. As for TiO1 and TiO2, the index increases with $[\alpha/Fe]$. However, this dependence is not compensated by an anticorrelation with [C/Fe], as the index is also expected to increase with carbon abundance (see the pink and green solid curves in Fig. A1). Notice that since the radial trends of $[\alpha/Fe]$ and [C/Fe] are rather flat in XSG1, based on CvD12 model predictions, one would not expect any gradient of aTiO throughout the galaxy. The strong radial variation of aTiO in Fig. A1 seems thus unexplained. This is further shown in Fig. A2, where open circles plot line strengths corrected to the solar scale with CvD12 models. One can explain the innermost corrected value with MIUSCAT models but there is no model prediction matching the outermost data points. However, one should consider that (i) CvD12 predictions for varying abundance ratios are only available for SSPs with solar metallicity and a Chabrier IMF. In practice, the effect of $[\alpha/Fe]$ and [C/Fe] might be dependent on metallicity and IMF; (ii) aTiO is a broad feature, and its sensitivity to [C/Fe] may be more uncertain, as it is entirely due to a variation of the continuum in the CvD12 models (see the green dashed line in Fig. A2); (iii) in

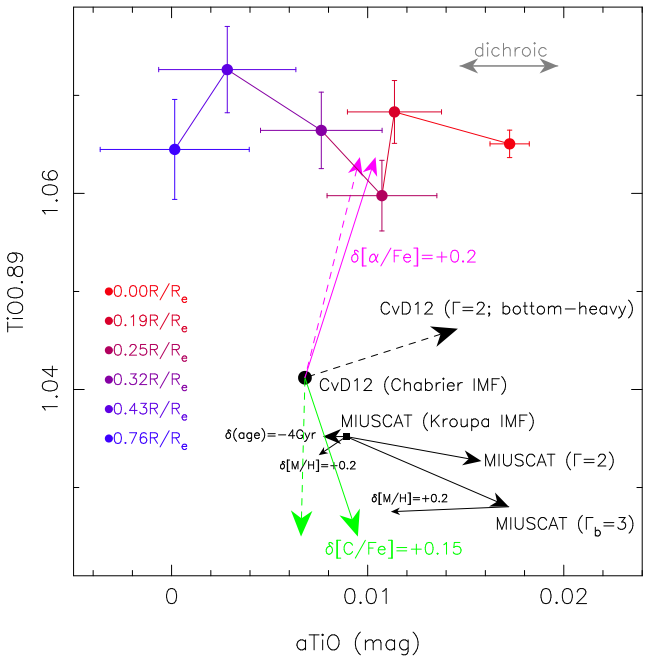

Figure A1. Same as in Fig. 8 but plotting TiO0.89 as a function of the aTiO IMF-sensitive feature. Pink and green dashed arrows show the sensitivity of TiO0.89 and aTiO to $[\alpha/Fe]$ and [C/Fe], respectively, when removing the continuum from CvD12 models. The black two-sided arrow in the top right of the plot shows the uncertainty in the absolute value of aTiO because of the time-variable response of the dichroic of the X-shooter spectrograph in the VIS arm.

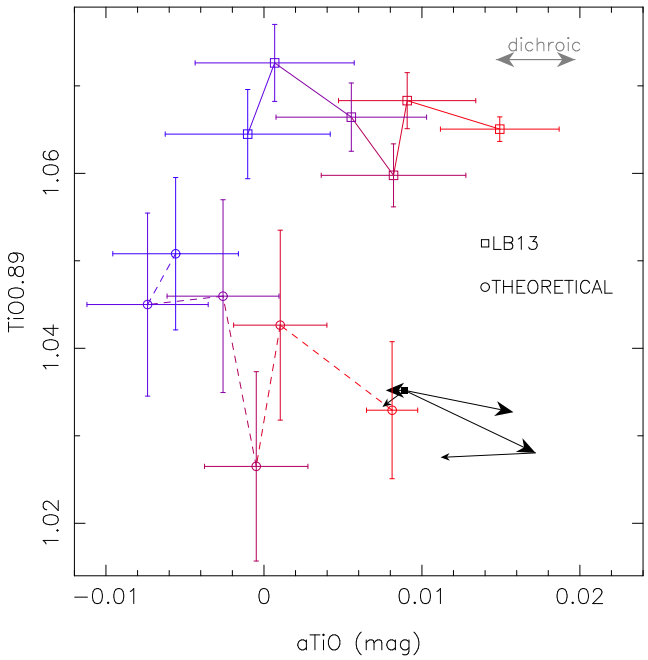

Figure A2. Same as in Fig. A1 but (i) correcting aTiO and TiO0.89 for their expected sensitivity to [α/Fe] and [C/Fe] (see circles and dashed line), and (ii) correcting aTiO for its SDSS-based sensitivity to abundance ratios, as in LB13 (see squares and solid line).

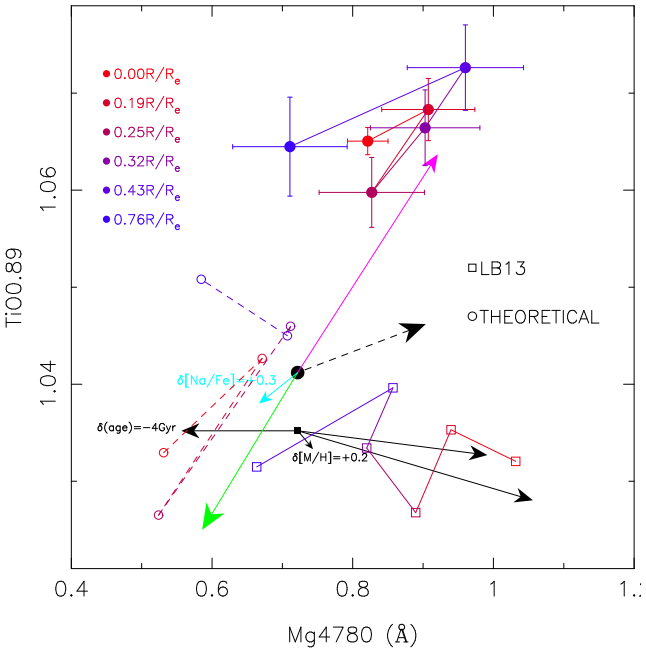

Figure A3. Same as in Fig. 8 but plotting TiO0.89 as a function of the Mg4780 IMF-sensitive feature. The cyan arrow shows the sensitivity of Mg4780 on [Na/Fe], based on CvD12 SSP models.

our data, the absolute value of aTiO is affected by the time-varying response of the UVB–VIS X-shooter dichroic. We measured this effect by computing the rms of aTiO values, in the central spectrum of XSG1, among different exposures (see the grey double-sided arrow at top right of Fig. A2). To gain insight into these issues, we also plot in Fig. 13 the empirically abundance-corrected values of aTiO (see the open squares in the figure). Indeed, following the approach of LB13, we find that, independently of the bin in velocity dispersion from the SDSS spectra, aTiO increases with [α/Fe], as $\delta_{\rm aTiO} = \delta({\rm aTiO})/\delta(\alpha/{\rm Fe}) \sim 0.006\,{\rm mag\,dex^{-1}}$. This implies a shift of $\sim-$ 0.0025 mag (for [α/Fe] $\sim$ 0.4) for all, but the outermost, uncorrected values of aTiO (Fig. A1). However, the value of $\delta_{\rm aTiO}$ might be underestimated for the innermost data points of XSG1. At fixed velocity dispersion in the SDSS data, there is also a mild increase ($\sim$0.1 dex) of metallicity with [α/Fe] – an effect that we have removed following LB13, by subtracting off the index variation expected from the change in metallicity for Kroupa-like MIUSCAT models (see section 5 of LB13). While this is correct for indices whose sensitivity to [M/H] does not depend on IMF (e.g. TiO1 and TiO2), it is not for aTiO. Accounting for this effect would make our empirical correction larger, by a factor of $\sim$3, in the innermost point of XSG1, implying the corrected value of aTiO in the centre to be $\sim$0.01 mag, in very good agreement with results from our best-fitting procedure to applied all optical indices (Section 5.3; Fig. 11). In summary, we think that the large radial gradient of aTiO in our target galaxy is a combination of (1) an underestimation of our empirical correction at high metallicity (we are currently working to improve method in this regard), and (2) the uncertainty in the zero-point of the index due to the dichroic response. Regarding point (1), it does not affect our results (see Section 5.3), whereas for point (2), we are currently working to improve the treatment of the dichroic issue in the reduction procedure. For the present work, we have decided to simply add in quadrature the uncertainty on the dichroic response to the observed error bars on aTiO.

A2 The Mg4780index

Fig. A3 plots the TiO0.89 as a function of Mg4780. Interestingly, no measurable radial gradient is found in Mg4780. The index tends to increase radially, from the innermost to the second outermost bin, while the outermost bin value is fully consistent with the central one (see the blue and red solid circles in the figure). Using CvD12 models, we find that the line strength of Mg4780 is expected to increase with [α/Fe] (mostly because of the sensitivity to [Mg/Fe], consistent with Serven, Worthey & Briley 2005) and decrease with [C/Fe], similarly to TiO1 and TiO2. Subtracting off the expected variation of the index from our [α/Fe] and [C/Fe] estimates (Fig. 7) with CvD12 models, we obtain the 'theoretically corrected' values (open circles) in Fig. A3, still showing (as expected) no significant radial gradient. Notice that the theoretically corrected line strengths are only consistent with a Kroupa-like IMF (especially in the innermost bin) and an age of $\sim$10–11 Gyr, inconsistent with results for TiO1 and TiO2. MN15a already noticed that Mg4780 is also dependent (to a lesser extent than [α/Fe] and [C/Fe]) on other single-element abundance ratios, i.e. [Na/Fe] and [Si/Fe]. In particular, Mg4780 is expected to be *anticorrelated* with [Na/Fe] because of its sensitivity to sodium on the blue pseudo-continuum, as illustrated by the cyan arrow in Fig. A3. Hence, a large [Na/Fe] radial gradient would tend to cancel out the effect of an IMF gradient on Mg4780. The open squares in Fig. A3 illustrate the results of our empirical correction procedure. As discussed in LB13, quite unexpectedly, the index tends to increase with [α/Fe] in the SDSS stacks at the lowest velocity dispersion (metallicity), while it *decreases* with [α/Fe] at the other end. As a result, the range of values for Mg4780 as a function of σ (see panel b in Fig. 8 of LB13) is significantly larger at high [α/Fe], than at [α/Fe] $\sim$ 0. This is fully consistent with the fact that, at such high [α/Fe] ($\sim$0.4), as is the case in XSG1, we do not see any radial gradient in Mg4780. Furthermore, in the massive ETG analysed in MN15a we saw Mg4780 to feature a shallower radial gradient than other IMF

indicators (mostly TiO2). Remarkably, our empirical correction – performed as a function of metallicity – recovers a clear radial gradient in XSG1, with values fully consistent with those obtained from the other optical indicators (see Section 5.3). Perhaps, the inconsistency between theoretical and empirical corrections for Mg4780 arises from the fact that some other elements (e.g. sodium) also give a prominent contribution to the observed line strengths, and/or the fact that the effect of $[\alpha/\mathrm{Fe}]$ and $[\mathrm{C}/\mathrm{Fe}]$ is strongly dependent, for this index, on $[M/\mathrm{H}]$ – something that cannot be tested with the available CvD12 models.

This paper has been typeset from a TEX/LATEX file prepared by the author.